

Structural and magnetic properties of the single-layer manganese oxide $\text{La}_{1-x}\text{Sr}_{1+x}\text{MnO}_4$

S. Laroche,^{1,*} A. Mehta,² L. Lu,³ P. K. Mang,³ O. P. Vajk,^{1,†}
N. Kaneko,^{2,‡} J. W. Lynn,⁴ L. Zhou,^{2,§} and M. Greven^{2,3}

¹*Department of Physics, Stanford University, Stanford, CA 94305*

²*Stanford Synchrotron Radiation Laboratory, Stanford Linear Accelerator Center, Stanford, CA 94309*

³*Department of Applied Physics, Stanford University, Stanford, CA 94305*

⁴*NIST Center for Neutron Research, National Institute of Standards and Technology, Gaithersburg, MD 20899*

(Dated: June 13, 2018)

Using x-ray and neutron scattering, we have studied the structural and magnetic properties of the single-layer manganite $\text{La}_{1-x}\text{Sr}_{1+x}\text{MnO}_4$ ($0 \leq x < 0.7$). Single crystals were grown by the traveling-solvent floating-zone method at 18 La/Sr concentrations. The low-temperature phase diagram can be understood by considering the strong coupling of the magnetic and orbital degrees of freedom, and it can be divided into three distinct regions: low ($x < 0.12$), intermediate ($0.12 \leq x < 0.45$), and high ($x \geq 0.45$) doping. LaSrMnO_4 ($x = 0$) is an antiferromagnetic Mott insulator, and its spin-wave spectrum is well-described by linear spin-wave theory for the spin-2 square-lattice Heisenberg Hamiltonian with Ising anisotropy. Upon doping, as the e_g electron concentration ($1 - x$) decreases, both the two-dimensional antiferromagnetic spin correlations in the paramagnetic phase and the low-temperature ordered moment decrease due to an increase of frustrating interactions, and Néel order disappears above $x_c = 0.115(10)$. The magnetic frustration is closely related to changes in the e_g orbital occupancies and the associated Jahn-Teller distortions. In the intermediate region, there exists neither long-range magnetic nor superstructural order. Short-range-correlated structural “nanopatches” begin to form above $x \sim 0.25$. At high doping ($x \geq 0.45$), the ground state of $\text{La}_{1-x}\text{Sr}_{1+x}\text{MnO}_4$ exhibits long-range superstructural order and a complex (CE-type) antiferromagnetic order which differs from that at low doping. The superstructural order is thought to arise from charge and orbital ordering on the Mn sites, and for $x = 0.50$ we conclude that it is of $B2mm$ symmetry. For $x > 0.50$, the superstructural order becomes incommensurate with the lattice, with a modulation wavevector ϵ that depends linearly on the e_g electron concentration: $\epsilon = 2(1 - x)$. On the other hand, the magnetic order remains commensurate, but loses its long-range coherence upon doping beyond $x = 0.50$.

PACS numbers: 61.10.Nz, 61.12.Ex, 61.12.Ld, 75.30.-m, 75.47.Lx

I. INTRODUCTION

The perovskite and perovskite-derived manganese oxides have attracted considerable interest over the last decade as the richness of their phase diagrams has been uncovered.^{1,2,3} Phases of interest include a ferromagnetic metallic phase, a paramagnetic phase with short-range structural distortions as well as several antiferromagnetic phases. The competition between the first two phases seems to play a key role in the colossal magnetoresistance (CMR) effect, while the presence of the other phases has renewed interest in the spin-orbital coupling issue in transition metal oxides.

The “single-layer” material $\text{La}_{1-x}\text{Sr}_{1+x}\text{MnO}_4$ is the $n = 1$ end-member of the Ruddlesden-Popper family $\text{La}_n(\text{1-x})\text{Sr}_{n\text{x}+1}\text{Mn}_n\text{O}_{3n+1}$ of manganese oxides. $\text{La}_{1+x}\text{Sr}_{1-x}\text{MnO}_4$ does not exhibit CMR^{4,5} and its layered structure results in strongly anisotropic transport properties.⁶ A magnetic/charge/orbital ordered phase is observed at low temperature at half doping ($x = 0.50$).^{7,8} The low dimensionality makes $\text{La}_{1+x}\text{Sr}_{1-x}\text{MnO}_4$ an interesting model system for the study of the underlying doped MnO_2 planes and for a comparison with results for the double-layer ($n = 2$) and perovskite ($n = \infty$) man-

ganites. Furthermore, $\text{La}_{1-x}\text{Sr}_{1+x}\text{MnO}_4$ is a structural homologue of the cuprate $\text{La}_{2-x}\text{Sr}_x\text{CuO}_4$ and the nickelate $\text{La}_{2-x}\text{Sr}_x\text{NiO}_4$ for which, in part because of their low dimensionality, the issue of charge inhomogeneity has been central in recent investigations.^{9,10} The most frequently studied composition of the single-layer manganites is $\text{La}_{0.50}\text{Sr}_{1.50}\text{MnO}_4$ ($x = 0.50$), although research also has extended to other La/Sr doping ratios^{4,5,11,12} and to $(\text{Nd,Sr})_2\text{MnO}_4$ and $(\text{Pr,Sr})_2\text{MnO}_4$.^{13,14,15,16}

At room temperature, $\text{La}_{0.50}\text{Sr}_{1.50}\text{MnO}_4$ has a highly symmetric body-centered tetragonal structure (space group $I4/mmm$ ¹⁷) which becomes strongly distorted at low temperature. The low-temperature structural phase was first observed by electron microscopy, which revealed a $(\frac{1}{4}, \frac{1}{4}, 0)$ wavevector modulation of the room temperature structure below ~ 220 K.^{4,5} An anomaly in the resistivity at this temperature indicates that the structural transition is associated with charge ordering. The existence of a distinct low-temperature phase was confirmed in a neutron scattering experiment,⁷ although it was concluded that this phase has a higher structural symmetry, with a $(\frac{1}{2}, \frac{1}{2}, 0)$ modulation of the room-temperature structure. This experiment also established the presence of antiferromagnetic order below 110 K. Based on the model originally developed by Goodenough¹⁸ for the

half-doped perovskite $\text{La}_{0.50}\text{Ca}_{0.50}\text{MnO}_3$ ($n = \infty$), these results were interpreted as an indication of charge order in $\text{La}_{0.50}\text{Sr}_{1.50}\text{MnO}_4$. Resonant x-ray scattering involves virtual excitations from core to valence states and thus can probe anisotropies in the valence charge density. A study of Mn K -edge resonant scattering from $\text{La}_{0.50}\text{Sr}_{1.50}\text{MnO}_4$ revealed a strong enhancement of the low-temperature superlattice peaks, which was interpreted as a confirmation of orbital and charge order in this compound.⁸ However, this interpretation has been controversial.^{19,20,21,22,23} The K -edge resonance involves virtual excitations to the unoccupied $4p$ levels, and thus is only an indirect probe of $3d$ states, and the signal is expected to be sensitive to both the lattice distortion and the atomic configuration. Recent soft x-ray scattering experiments at the Mn L edge^{24,25,26} might be better evidence of orbital ordering since they directly probe the $3d$ states, and it has been suggested that it is possible to spectroscopically differentiate cooperative Jahn-Teller distortions of the Mn^{3+} ions and direct (or spin-correlation-driven) orbital ordering.^{24,25} In another study,²⁷ related linear dichroism results at the Mn L edge were interpreted as evidence that the e_g orbital order in the CE phase involves $d_{x^2-z^2}$ and $d_{y^2-z^2}$ orbitals rather than the $d_{3x^2-r^2}$ and $d_{3y^2-r^2}$ orbitals, as is generally assumed. However, the two ordering patterns share the same lattice symmetry. Finally, from a consideration of the number of allowed Raman modes, the orthorhombic $Pbmm$ symmetry was proposed for the low-temperature phase,²⁸ which would manifest itself in a $(\frac{1}{4}, \frac{1}{4}, 0)$ modulation of the room-temperature structure.

The phase transition at $x = 0.50$ also causes changes in the optical properties of the material. Infrared absorption²⁹ and reflectivity³⁰ measurements reveal that the optical gap increases significantly below the transition temperature. Moreover, the material becomes birefringent in the low-temperature phase³¹ as a result of the orthorhombic distortion caused by the orbital order. The low-temperature phase is fragile and can be destroyed by magnetic fields of ~ 25 T.³² Furthermore, photo-induced melting of the charge/orbital phase with exposure of the sample to 1.55 eV laser light has been reported.³³ We will present results in this paper that are indicative of a partial x-ray induced melting in the ordered phase, similar to what was reported previously for $\text{Pr}_{0.30}\text{Ca}_{0.70}\text{MnO}_3$ ³⁴ and $\text{La}_{0.875}\text{Sr}_{0.125}\text{MnO}_3$.³⁵

Compared to the efforts made to study the lattice distortions associated with the insulating behavior, relatively little is known about the magnetic properties of the single-layer manganites. Magnetization,⁶ muon spin rotation³⁶ and neutron scattering^{7,37,38,39} measurements have established that $\text{La}_{1-x}\text{Sr}_{1+x}\text{MnO}_4$ is an antiferromagnet near $x = 0$, $x = 0.5$ and $x = 1$, with Néel temperatures of about 120 K, 110 K and 170 K, respectively. At $x = 0$ and $x = 1$, the magnetic structure is antiferromagnetic in the MnO_2 planes, with spins aligned parallel to the stacking direction. At half-doping, on the other hand, the magnetic structure is related to the complex CE mag-

netic phase of the perovskite manganites and is composed of two interpenetrating lattices of (antiferromagnetically-coupled) ferromagnetic zigzag chains. The spins in this case lie within the MnO_2 planes. Finally, we note that there have been reports^{4,36,40,41} of glassy magnetic behavior at low temperature between dopings of $x = 0.20$ and $x = 0.60$.

In a previous Letter,¹² we examined the nature of the e_g electron order in $\text{La}_{1-x}\text{Sr}_{1+x}\text{MnO}_4$. We briefly described the low-temperature phase at doping $x = 0.50$ and reported on the observation of an incommensurate lattice distortion for $x > 0.50$. The present paper is organized as follows: after describing our experimental methods in Sec. II, we present our magnetic neutron scattering results for the magnetic phase at low doping ($0 \leq x \leq 0.15$) in Sec. III. In Sec. IV, we then discuss the structural and magnetic properties of the low-temperature phase that is present in the doping range $0.45 \leq x < 0.7$. Section V describes the short-range structural and magnetic correlations observed in the intermediate doping range $0.15 < x < 0.45$. Finally, Sec. VI presents the magnetic and structural phase diagram of $(\text{La,Sr})_2\text{MnO}_4$ and a discussion of our results.

II. EXPERIMENTAL METHODS

In order to obtain single crystals, stoichiometric amounts of La_2O_3 , SrCO_3 and MnO_2 (99.99% purity or higher) were mixed and calcinated three times for thirty-six hours in an alumina crucible at temperatures of 1300-1360°C, with intermediate grinding. The reacted and ground powder was then pressed into cylindrical rods and sintered for twelve hours in air at 1500-1580°C. Crystals were grown from the ceramic rods using a four-mirror optical image furnace at a speed of 6 mm per hour. Prior to the growth, the ceramic rods were rapidly sintered inside the image furnace at about 85% of the power needed to melt them. A total of 24 crystals were grown at 18 different compositions, ranging from $x = 0.00$ to $x = 0.67$, which is close to the solubility limit of $x \approx 0.70$.^{4,5} The growth atmosphere varied from argon (partial pressure of oxygen of $\sim 10^{-6}$ bar) for $x = 0.00$ compound up to 6 bar atmosphere of O_2 for samples with $x = 0.67$.

For the x-ray measurements, crystal pieces of about $4 \times 2 \times 1$ mm³ were cut from the boule and mounted inside a displax. Single crystal x-ray measurements were performed on beam line 7-2 at the Stanford Synchrotron Radiation Laboratory (SSRL). An energy of 14 keV was selected from the wiggler spectrum with a double-crystal Si(111) monochromator. Additional high-resolution powder x-ray scattering measurements were performed on SSRL beam line 2-1. Single crystal pieces were finely ground and the resulting powder was packed into a cavity in a silicon zero-background (510) mount. The samples were mounted and cooled in a transfer helium gas cryostat. The high momentum resolution was achieved by using a Si(220) double-crystal monochro-

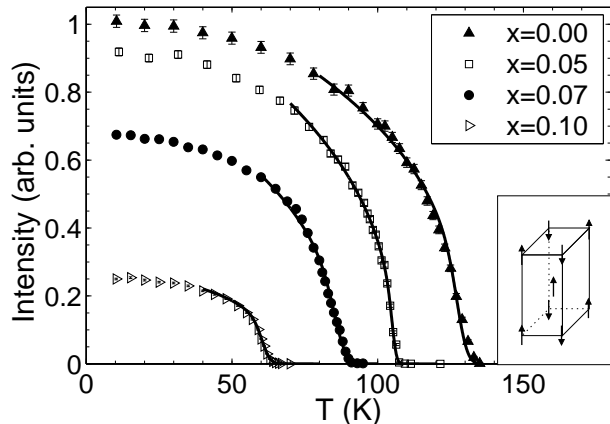


FIG. 1: $\text{La}_{1-x}\text{Sr}_{1+x}\text{MnO}_4$ magnetic Bragg scattering intensity as a function of temperature, measured at the reciprocal space positions $(1,0,4)_m$ for $x = 0.00$, $(1,0,0)_m$ for $x = 0.05$, and $(1,0,3)_m$ for $x = 0.07$ and 0.10 . The subscript "m" indicates the unit cell of the magnetic structure shown in the inset. The intensity is normalized by the size of the crystals, and the low-temperature value for $x = 0.00$ was set to 1. The lines are fits to the form $I \sim (1 - T/T_N)^{2\beta}$ assuming a Gaussian distribution in Néel temperatures due to sample inhomogeneity. The values of T_N , β , and the ordered moment are listed in Table I.

mator and a Si(111) analyzer. Single-crystal neutron scattering measurements were carried out on the thermal triple-axis instruments of the NIST Center for Neutron Research (NCNR).

III. MAGNETIC ORDER AND SPIN CORRELATIONS ($0 \leq x < 0.15$)

The Néel phase of LaSrMnO_4 ($x = 0$) was studied previously by several groups.^{4,36,38,39,42} These experiments found that LaSrMnO_4 orders antiferromagnetically with the K_2NiF_4 spin structure, an Ising anisotropy, and moments aligned along $[0,0,1]$. In four of the five experiments the Néel temperatures were determined to be between 120 K and 130 K, while $T_N = 180$ K was reported in Ref. 38. In this Sec., we present neutron scattering measurements of the spin-wave dispersion for $x = 0$, and of the order parameter and instantaneous spin-spin correlation lengths for samples in the doping range $0 \leq x \leq 0.15$. The goal of these measurements is to further establish the properties of the magnetic phase of LaSrMnO_4 and to study its evolution upon doping.

Our results for the magnetic structure of LaSrMnO_4 are in good agreement with the earlier powder neutron diffraction studies.^{38,39} The observed magnetic peaks can be indexed using the proposed structure, with nearest-neighbor (NN) moments antiferromagnetically aligned within the Mn-O plane, and with next-NN planes stacked ferromagnetically (see inset of Fig. 1). The structure is

TABLE I: Néel temperature, ordered moment and order parameter critical exponent of $\text{La}_{1-x}\text{Sr}_{1+x}\text{MnO}_4$ ($0.00 \leq x \leq 0.10$). The value of the ordered moment for $x = 0.00$ is from Ref. 39. The values for other doping concentrations are derived from the relative values of the measured Bragg peak intensities, as discussed in the text.

x	T_N	$M_{st}(x)/M_{st}(0)$	$M_{st}(x)$	β
0.00	128.4(5)	1	$3.3(2)\mu_B$	0.18(3)
0.05	105.5(2)	0.95(8)	$3.1(4)\mu_B$	0.20(3)
0.075	86.5(2)	0.82(6)	$2.7(4)\mu_B$	0.20(4)
0.10	61.0(5)	0.50(4)	$1.6(2)\mu_B$	0.13(4)

twinned, because the magnetic order of the intermediate Mn-O plane is not constrained by its two neighboring planes (the center Mn spin can point either up or down) and peaks corresponding to both twin domains were observed. No additional antiferromagnetically-stacked phase (observed, for example, in Rb_2MnF_4 ⁴³) is discernible to a level of 200 ppm. An antiferromagnetically-stacked phase would result in a Bragg peak with $L = 0.5$ r.l.u., for example. No changes in the magnetic structure were noticed upon doping up to $x = 0.10$.

The order parameter of samples in the antiferromagnetic phase was determined by measuring the temperature dependence of the intensity of one of the magnetic peaks, as shown in Fig. 1. The Néel temperature for the undoped sample is 128.4(5) K, in good agreement with four of the five previous measurements.^{4,36,39,42} The transition shows some rounding, most likely the result of chemical inhomogeneities from La-Sr substitutions. Allowing for a Gaussian distribution of the Néel temperature, we obtained $\beta = 0.18(3)$ for the order parameter critical exponent of LaSrMnO_4 ($x = 0$) from the fit shown in Fig. 1. This value of β is similar to those of other two-dimensional Heisenberg antiferromagnets with an Ising anisotropy, and within two standard deviations of the 2D Ising value $\beta = 0.125$.⁴⁴ As discussed in detail below, the spin-wave spectrum features a relatively large Ising anisotropy gap. Consequently, even though the rounding is not small, the extracted exponent is consistent with the presence of a significant Ising anisotropy. We note that the rounding ΔT_N (half-width-at-half-maximum) is $\Delta T_N/T_N = 1.5 - 4\%$ in the four samples with $x \leq 0.10$. For example, for the $x = 0.10$ sample, this corresponds to doping inhomogeneities of less than $\Delta x = 0.003$.

As a next step, we studied the evolution of the antiferromagnetic order upon doping. In Fig. 1, the magnetic Bragg scattering intensities are scaled relative to each other based on data for the peak intensities that were normalized per mole. The ordered staggered moment, $M_{st}(x)$, is proportional to the square root of the low-temperature intensity. Only relative moments were measured in this experiment. Previous powder scattering measurements indicate that the ordered moment at $x = 0.00$ is $3.3(2)\mu_B$.³⁹ Establishing the ab-

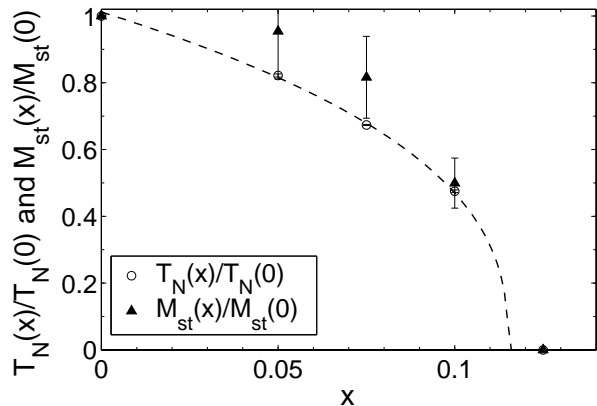


FIG. 2: Néel temperature and ordered moment (measured at $T = 10$ K) as function of doping for $\text{La}_{1-x}\text{Sr}_{1+x}\text{MnO}_4$. The values are normalized to those of the $x = 0.00$ sample. The dashed line is a guide to the eye for the doping dependence of the Néel temperature, indicating our estimate of $x_c = 0.115(10)$ for the disappearance of two-dimensional long-range order.

solute value of the ordered moments from single-crystal measurements requires a quantitative comparison of the intensities of the magnetic Bragg peaks to those of nuclear peaks. Accurate measurements of nuclear peak intensities are difficult because the strong peaks generally suffer from extinction while the intensity of the weak nuclear peaks critically depends on the exact position of the atoms. One solution is to use small crystals which would limit the extinction of the strong nuclear peaks. This was not pursued as it would have hindered the correlation length measurements on the same samples (discussed below) for which the signal is much smaller. Another possibility would be to normalize the magnetic intensities by that of an acoustic phonon. As stated above, the ordered moment has been determined with good accuracy for $x = 0.00$.³⁹ Given that the magnetic structure was found to stay the same up to $x = 0.10$, we were able to pursue a third approach, the normalization of the magnetic intensities per unit volume for $0 < x \leq 0.10$ to the value determined previously for $x = 0.00$.

We observed (two-dimensional) long-range order up to $x = 0.10$. Figure 2 shows the evolution of the Néel temperature and staggered ordered moment as a function of doping. We estimate that antiferromagnetic order disappears at $x_c = 0.115(10)$. The ordered moment decreases approximately linearly with the Néel temperature. Table I reports the Néel temperature as well as the absolute and relative moments at $T = 10$ K. The magnetic Bragg peaks of LaSrMnO_4 are resolution limited in both in-plane and out-of-plane directions, indicating three-dimensional long-range order, within the experimental precision. We note that the $x = 0.10$ sample was not fully three-dimensionally ordered at 10 K, the base temperature of our experiment, since Lorentzian broad-

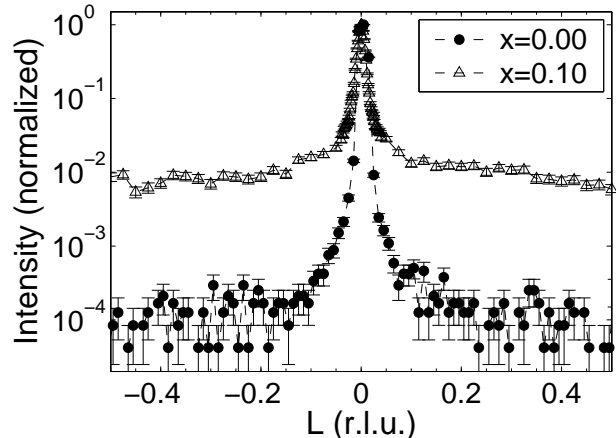


FIG. 3: L -scans at $T = 10$ K through the $(1,0,0)_m$ magnetic Bragg peak for $x = 0$ and 0.10 , normalized at the peak position. For $x = 0$, the peak is resolution limited, indicating three-dimensional long-range order, while it is broader than resolution for $x = 0.10$. Away from the $(1,0,0)_m$ peak, the diffuse scattering is two orders of magnitude higher for the $x = 0.10$ sample. The extra intensity is due to a rod of two-dimensional scattering. The data were taken on the spectrometer BT7 with 13.4 meV neutrons and collimations of $35' - 40' - \text{sample} - 25.8' - \text{open}$.

ening and a rod of two-dimensional scattering were discernible along $[0, 0, 1]$. This is demonstrated in Fig. 3. Samples with higher doping ($x \geq 0.125$) only showed two-dimensional short-range correlations at 10 K. The temperature dependence of the two-dimensional spin-spin correlation length in the paramagnetic phase will be described in detail below.

Reutler *et al.*⁴² reported long-range order for $x = 0.125$. This discrepancy with our result most likely stems from a difference in the oxygen content, since the crystal studied in Ref. 42 was grown under more reducing conditions (CO_2) than in the present study (air). From a comparison of the Néel temperatures, the oxygen stoichiometry difference between the two samples can be estimated to be about $\delta = 0.015$.

In order to establish the local magnetic parameters of LaSrMnO_4 , we measured the low-temperature spin waves along the principal crystallographic directions: $(\zeta, 0, 0)_m$, $(\zeta, \zeta, 0)_m$, $(0.5, \zeta, 0)_m$ and $(0, 0, \zeta)_m$ (the reciprocal lattice considered in this Sec. corresponds to the magnetic unit cell described previously). We carried out fixed-momentum scans, varying the incident neutron energy. Example scans are shown in Fig. 4. In order to fit the data, a Lorentzian cross section was convoluted with the spectrometer resolution function using the program ResLib.⁴⁵ Since the convolution depends on the shape of the dispersion curve, the fit procedure was iterated several times, each time including the result for the dispersion from the previous iteration. Convergence was reached after three iterations. The magnetic excitations are not resolution limited and they broaden significantly

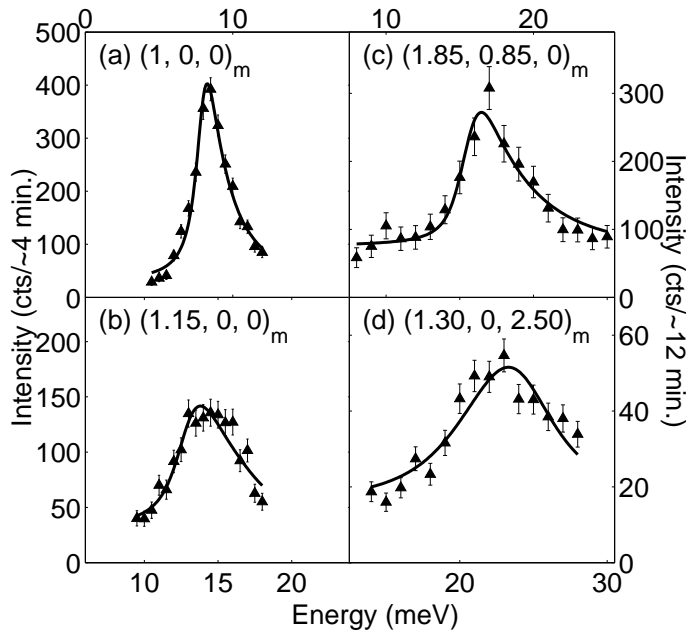


FIG. 4: LaSrMnO₄ spin waves at 10 K. The lines are fits of the spin-wave dispersion curve (assuming a Lorentzian cross section) convoluted with the resolution function of the neutron spectrometer. The data were taken on the spectrometer BT2 with 14.7 meV final energy neutrons and collimations of 60'-40'-sample-40'-80'.

at higher wavevectors, from ~ 1 meV at the zone center to ~ 4 meV along the zone boundary. The broadening above ~ 20 meV might be due to a coupling between the spin-waves and optical phonons. A similar broadening was reported previously for the double-layer compound (La,Sr)₃Mn₂O₇ and was attributed to phonon-magnon coupling.^{46,47} The excitations are dispersionless along $[0, 0, 1]_m$, as is expected for a quasi-two-dimensional magnet.

Our data for the spin-wave dispersion, summarized in Fig. 5, demonstrate that the magnetic degrees of freedom of LaSrMnO₄ are described to a good approximation by the two-dimensional square-lattice Hamiltonian

$$\mathcal{H} = J_1 \sum_{\langle i,j \rangle_1} (S_i^x S_j^x + S_i^y S_j^y + (1 + \alpha) S_i^z S_j^z) + J_2 \sum_{\langle i,j \rangle_2} (S_i^x S_j^x + S_i^y S_j^y + S_i^z S_j^z), \quad (1)$$

where J_1 and J_2 are, respectively, the NN and second-NN Heisenberg exchange couplings, and α is the Ising anisotropy. The sums run over first ($\langle i, j \rangle_1$) and second ($\langle i, j \rangle_2$) nearest neighbors. The parameters J_1 , J_2 and α of this Hamiltonian can be extracted by modeling the dispersion of the low-temperature spin-wave spectrum with the predictions from linear spin-wave theory. For the Hamiltonian Eq. (1), the spin-wave dispersion is given

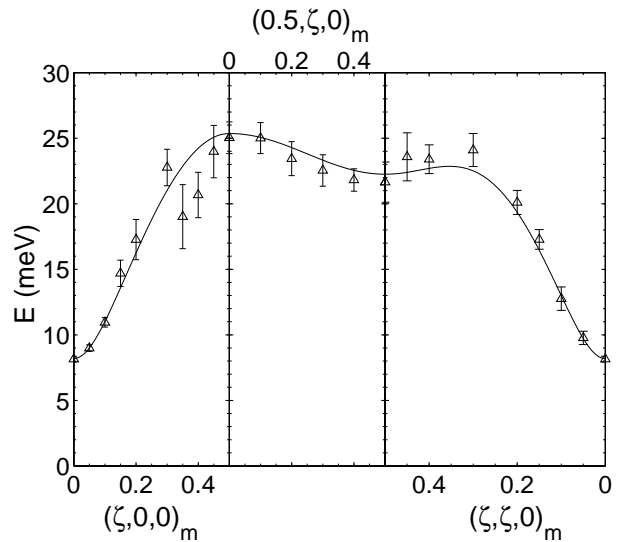


FIG. 5: LaSrMnO₄ spin-wave dispersion at 10 K. The line is Eq. (2) with parameters $J_1 = 3.4(3)$ meV, $\alpha = 0.044(6)$ and $J_2/J_1 = 0.11(3)$.

by

$$E(\mathbf{q}) = 4SZ_c J_1 \sqrt{\left(1 + \alpha + \frac{1}{2} \frac{J_2}{J_1} \gamma_2(\mathbf{q})\right)^2 - \gamma_1(\mathbf{q})^2} \quad (2)$$

$$\gamma_1(\mathbf{q}) = \cos\left(\frac{1}{2} q_x a_m\right) \cos\left(\frac{1}{2} q_y a_m\right)$$

$$\gamma_2(\mathbf{q}) = \cos(q_x a_m) + \cos(q_y a_m) - 2,$$

where Z_c is a quantum renormalization factor (for spin 2, $Z_c \approx 1.04$). The NN coupling J_1 affects mostly the slope of the dispersion near the zone center, while the anisotropy α results in an energy gap at the zone center. A non-zero value of J_2 causes a dispersion along the zone boundary (along $[\frac{1}{2}, K, 0]_m$). Overall, the dispersion is not very sensitive to higher-order corrections such as J_2 , and it is generally not possible to extract more than one independent higher-order parameter. J_2 should thus be seen as an effective parameter that contains all the high-order (that is, beyond NN) contributions. The three-parameter fit in Fig. 5 provides a good description of our data, and we obtain $J_1 = 3.4(3)$ meV, $\alpha = 0.044(6)$ and $J_2/J_1 = 0.11(3)$. We note that for the $S = 1/2$ NN square-lattice Heisenberg antiferromagnet quantum fluctuations lead to a $\approx 7\%$ dispersion along the zone boundary.^{48,49} In the $S = 2$ case, however, quantum effects are expected to be significantly smaller, and the zone boundary dispersion observed for LaSrMnO₄ is dominated by the next-NN exchange J_2 .

The value $\alpha = 0.044$ is quite large, and this results in a surprisingly large anisotropy gap of about 8 meV. The anisotropy is an order of magnitude larger than for model Heisenberg magnets such as Rb₂MnF₄ ($\alpha = 0.0048$, Ref. 50) or K₂NiF₄ ($\alpha = 0.0021$, Ref. 51). However, it is

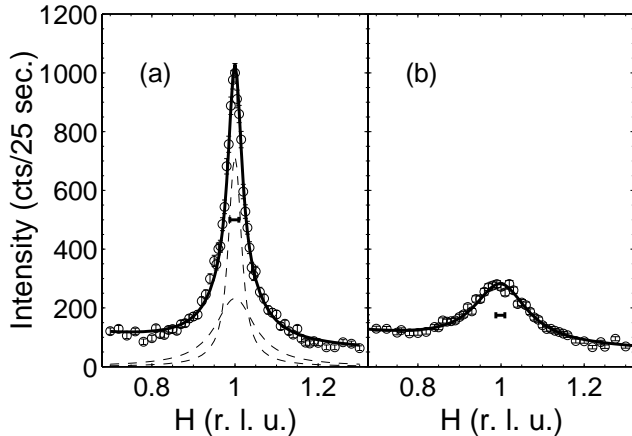


FIG. 6: Examples of energy-integrating two-axis scans of the instantaneous magnetic structure factor in the disordered phase of LaSrMnO_4 . Scan (a) was taken at $T = 131.5$ K, in the temperature range just above the Néel temperature ($T_N = 128.4(5)$ K) where the Ising anisotropy is important. The two dashed lines are the contributions from the parallel (narrower peak) and perpendicular (broader peak) components. Scan (b) was taken at $T = 160$ K where the system behaves as an isotropic two-dimensional Heisenberg antiferromagnet. The horizontal bars indicate the instrumental resolution. The data were taken on the spectrometer BT7 with 13.4 meV initial energy neutrons and collimations of $35' \text{-} 40' \text{-} \text{sample} \text{-} 25.8' \text{-} \text{open}$.

still much lower than in systems that show nearly ideal two-dimensional Ising behavior, such as Rb_2CoF_4 , where $\alpha = 0.81(8)$.⁵²

Having gained a good understanding of the ordered phase, we next measured the instantaneous antiferromagnetic correlations in the paramagnetic phase. In this phase, the magnetic scattering consists of rods at the antiferromagnetic wavevector positions in the $H-K$ plane. The scattering intensity is independent of the L position apart from a dependence on the magnetic form factor. Representative two-axis scans are shown in Fig. 6. We extracted the correlation length by folding the instantaneous magnetic structure factor $S(\mathbf{q})$ with the spectrometer resolution function. The structure factor has two components which correspond to the spins fluctuations parallel and perpendicular to the easy-axis ($[0,0,1]$), as described in Ref. 53:

$$S(\mathbf{q}_{2D}) = \sin^2(\phi) \frac{S_{\parallel}(0)}{1 + q_{2D}^2/\kappa_{\parallel}^2} + (1 + \cos^2(\phi)) \frac{S_{\perp}(0)}{1 + q_{2D}^2/\kappa_{\perp}^2} \quad (3)$$

where $\kappa_{\parallel(\perp)}$ is the inverse correlation length of the parallel (perpendicular) fluctuations, and ϕ is the angle between the scattering wavevector \mathbf{Q} and the \mathbf{c} axis. The quantity q_{2D} is the magnitude of the component of the reduced wavevector \mathbf{q} in the $H-K$ plane; \mathbf{q} is defined within

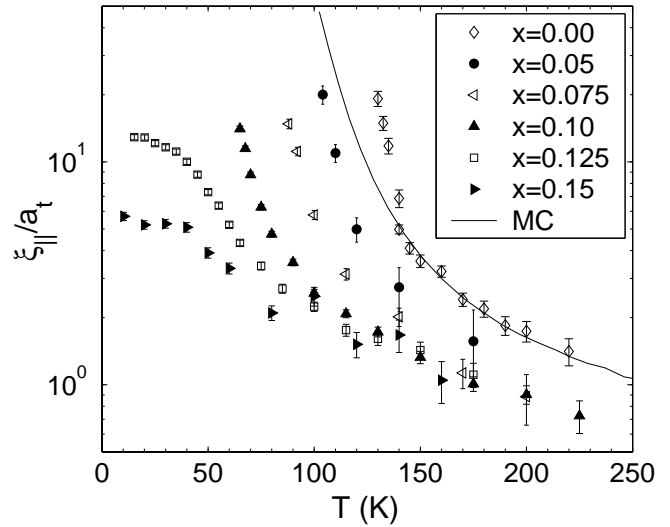


FIG. 7: Antiferromagnetic correlation length, in units of the tetragonal lattice constant a_t , as function of temperature in $\text{La}_{1-x}\text{Sr}_{1+x}\text{MnO}_4$. The line is the result of a Monte-Carlo simulation of the spin-2 NN square-lattice Heisenberg antiferromagnet with an exchange coupling of $J = 31.8$ K.

a Brillouin zone: $\mathbf{q} = \mathbf{Q} - \mathbf{G}$, where \mathbf{G} is the nearest reciprocal lattice vector. The ϕ -dependent prefactors in Eq. (3) originate from the fact that only the spin component perpendicular to the scattering wavevector contributes to the magnetic cross section for unpolarized neutrons. At temperatures well above the Néel temperature, the spin system is isotropic and the perpendicular and parallel components of the structure factor are indistinguishable. As the system is cooled toward the Néel temperature, the Ising anisotropy becomes relevant, and the system undergoes a crossover from two-dimensional Heisenberg to two-dimensional Ising behavior. At the Néel temperature, the correlation length of the parallel component diverges while that of the perpendicular component remains finite. An estimate of this finite perpendicular correlation length is available within the framework of linear spin-wave theory:⁵¹

$$\xi_{\perp}/a_m = \sqrt{Z_c/8\alpha} \quad (4)$$

where a_m is the in-plane lattice parameter of the magnetic unit cell. Using the value of α obtained through the measurement of the spin-wave spectrum for the $x = 0.00$ sample, $\xi_{\perp} = 9.7(9)$ Å at the Néel temperature. This value was used to fit the experimental data close to the Néel temperature since the fit was unstable if the parallel and perpendicular correlation lengths were both allowed to vary. The same value was used to analyze the data for $x = 0.05, 0.075$ and 0.10 .

Figure 7 shows the correlation length of the component of the magnetic fluctuations parallel to the easy-axis for

TABLE II: Effective spin stiffness and low-temperature correlation length for $x \leq 0.15$.

x	ρ_{eff} (K)	$\xi(x, 0)/a_t$
0.00	114(3)	–
0.05	91(5)	–
0.075	72(5)	–
0.10	51(4)	–
0.125	–	13.8(3)
0.15	–	5.6(2)

several dopings between $x = 0$ and $x = 0.15$. We also calculated the correlation length for the spin-2 NN square-lattice Heisenberg antiferromagnet using the loop-cluster Monte-Carlo method.⁵⁴ We obtain good agreement (solid line) with the data at $x = 0$ between 140 K and 250 K using an exchange coupling of $J = 31.8$ K (2.75 meV). At temperatures lower than 140 K, the Ising anisotropy becomes relevant, and the measured correlation length diverges more strongly than for the Heisenberg model. The exchange coupling obtained from the comparison with the numerical result is somewhat smaller than the value $J_1 = 3.4(3)$ meV obtained from the spin-wave dispersion curve. This discrepancy is probably due to the relatively strong frustrating second-NN coupling ($J_2 \approx 0.11J_1$) which will lower the spin correlations and was not considered in the simulation.

For the spin-5/2 materials Rb_2MnF_4 and KFeF_4 , it was found that the mean-field form⁵⁵

$$\xi(T) = \frac{\xi_H(T)}{\sqrt{1 - \alpha\xi_H^2(T)}}, \quad (5)$$

where $\xi_H(T)$ is the correlation length of the Heisenberg model, gives a good description of the crossover from Heisenberg to Ising spin correlations.⁵³ In the case of LaSrMnO_4 , this form does not capture the crossover, since the Ising anisotropy is an order of magnitude larger and, consequently, two-dimensional Ising critical effects are relevant over a wider reduced temperature range. While the mean-field result predicts a power-law exponent of $\nu = 1/2$ for the divergence of the correlation length, the proper two-dimensional Ising result is $\nu = 1$. We note that our data are insufficient to extract the correlation length exponent from experiment.

Upon doping, the magnetic correlation length $\xi(x, T)$ decreases at any given temperature. For $x < x_c$, a possible heuristic description is to consider this decrease to be primarily due to a change of the spin stiffness. As Elstner *et al.* have shown,⁵⁶ the correlation length for the spin- S NN square-lattice Heisenberg model falls on an approximately universal curve if one considers $\xi(\rho/Z_\rho)/(c/Z_c)$ as a function of $T/(\rho/Z_\rho)$, where ρ is the spin stiffness and c is the spin-wave velocity. Following this approach, and assuming that the quantum correction factors Z_ρ and Z_c are unaltered from their $S = 2$ values of ~ 1 ,⁵⁷ we extract an effective spin stiffness. For example, at $x = 0.10$

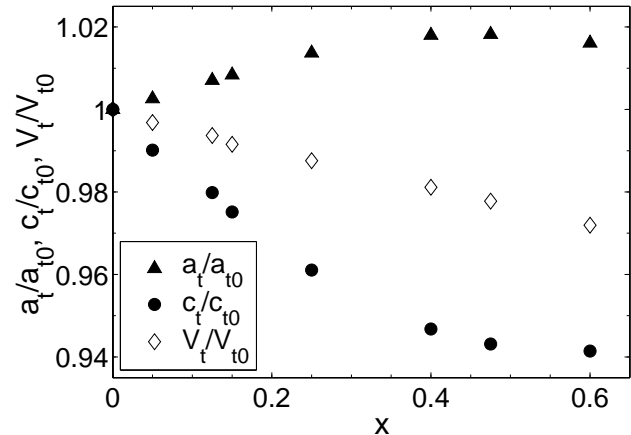


FIG. 8: Room-temperature lattice parameters and unit-cell volume of $\text{La}_{1-x}\text{Sr}_{1+x}\text{MnO}_4$ for the tetragonal unit cell, normalized to the $x = 0$ values: $a_{t0} = 3.796(4)$ Å, $c_{t0} = 13.18(2)$ Å, and $V_{t0} = 189.9(7)$ Å³. The unit-cell volume decreases linearly with doping. The in-plane lattice parameter a_t expands slightly while the out-of-plane lattice parameter c_t contracts significantly with doping.

we estimate that ρ_{eff} is about 40% of the $x = 0$ value. The values for ρ_{eff} are reported in Table II.

The spin stiffness becomes zero at $x = x_c$. For the structurally related compound $\text{La}_{2-x}\text{Sr}_x\text{CuO}_4$, a simple empirical relation was found to hold for $x > x_c$:⁵⁵

$$\xi^{-1}(x, T) = \xi^{-1}(0, T) + \xi^{-1}(x, 0). \quad (6)$$

This form does not describe the present situation since the correlation lengths for the short-range-ordered samples ($x = 0.125$ and 0.15) exhibit a significant temperature dependence already at intermediate temperatures. For $x = 0.125$ and 0.15 , Table II reports the estimated zero-temperature correlation length.

Magnetometry⁴ and muon-spin-rotation³⁶ measurements of $\text{La}_{1-x}\text{Sr}_{x+1}\text{MnO}_4$ suggest that the antiferromagnetic state near $x = 0$ is replaced by a spin-glass phase at intermediate doping. The presence of a spin-glass phase points toward a frustration-induced suppression of the Néel order. The frustration appears as the system evolves toward the $x = 0.50$ configuration in which the NN exchanges are ferromagnetic along zigzag chains and antiferromagnetic perpendicular to the chains. It has been established from studies of the Ising model with random ferromagnetic and antiferromagnetic bonds ($\pm J$),⁵⁸ and from studies of random mixtures of magnetic ions with both ferromagnetic and antiferromagnetic couplings,⁵⁹ that the presence of such random bonds in a (predominantly) NN magnet results in the destruction of the ordered magnetic ground state and its replacement by a spin-glass phase as the density of frustrating bonds increases.

In the case of manganites, the sign of the exchange integral between NN manganese ions can be related to the e_g orbital occupations and to the associated Jahn-Teller distortion by considering the coupling between spins and orbitals (see, for example, Ref. 1). We recall that the density of e_g electrons, and hence of nominal Mn^{3+} Jahn-Teller ions, is $1 - x$. In $\text{La}_{1-x}\text{Sr}_{1+x}\text{MnO}_4$, at $x = 0$, the Jahn-Teller distortions involve all Mn ions and are mostly along the z direction ($3z^2 - r^2$ orbitals), while at $x = 0.5$ most are within the $x - y$ plane ($3x^2 - r^2$ and $3y^2 - r^2$ orbitals¹⁸ or $x^2 - z^2$ and $y^2 - z^2$ orbitals²⁷) with half the sites (the “ Mn^{4+} ” sites) rather undistorted. The evolution of the lattice parameters indicates the trend of the occupation probability of the out-of-plane and in-plane Jahn-Teller orbitals. As shown in Fig. 8, our measurement of the room-temperature lattice parameters as a function of doping shows that the c lattice constant decreases by 5.7% between $x = 0$ and $x = 0.50$ while the a lattice constant increases by 2%. About 70% of the change in the lattice parameters occurs between $x = 0$ and $x = 0.25$. In that range, the distribution of the Jahn-Teller orbitals should be rather random since no correlated distortion of the lattice is observable (see Sec. V).

The location of the boundary between the antiferromagnetic and the spin-glass phases depends on the magnitude of the ferromagnetic (J_F) and antiferromagnetic (J_{AF}) couplings. From our spin-wave measurements for LaSrMnO_4 , we estimate J_{AF} is estimated to be 3.4 meV (J_1). However, the coupling between Mn ions with different types of Jahn-Teller distortions could be different. For the ferromagnetic coupling, an estimate can be obtained from the spin-wave measurements in the bilayer manganite $(\text{La,Sr})_3\text{Mn}_2\text{O}_7$.⁴⁷ Here, in the ferromagnetic state, the in-plane NN coupling is approximately -5 meV. Thus J_F likely is comparable to J_{AF} in the single-layer manganite. The situation for $\text{La}_{1-x}\text{Sr}_{1+x}\text{MnO}_4$ can be compared to another compound with site-induced frustration: $\text{Rb}_2\text{Cu}_{1-x}\text{Co}_x\text{F}_4$.⁶⁰ In that material, the coupling between copper sites is ferromagnetic ($J_{Cu-Cu} = -22.0$ K) and the other couplings are antiferromagnetic ($J_{Co-Co} = 90.8$ K and $J_{Cu-Co} \approx 9$ K). The magnetic ground state of the compound is a ferromagnet in the range $0 \leq x \leq 0.18$, an antiferromagnet for $0.40 \leq x \leq 1$ and a spin glass in the intermediate doping regime $0.18 < x < 0.4$. Since the antiferromagnetic phase disappears already at a lower critical doping level in $(\text{La,Sr})_2\text{MnO}_4$ ($x_c \approx 0.115(10)$), the frustration appears to be somewhat larger.

IV. THE CHARGE-ORDERED PHASE ($0.45 \leq x < 0.70$)

Many manganites at and near half doping exhibit a rather complex distortion of the lattice accompanied by magnetic order. This low-temperature phase, usually referred to as the CE phase, appears to depend only weakly

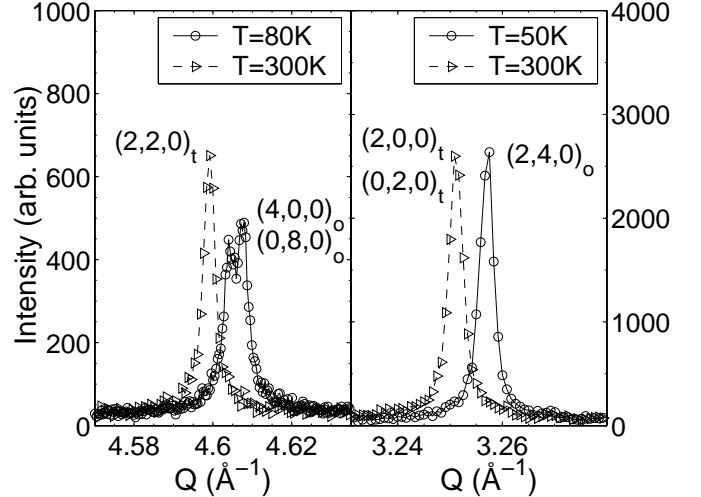


FIG. 9: Comparison of $\text{La}_{0.50}\text{Sr}_{1.50}\text{MnO}_4$ powder diffraction scans at room temperature and at low temperature. The scans show (a) the $(2, 2, 0)_t$ peak and (b) the $(2, 0, 0)_t$ peak. In the former case, the peak splits at low temperature, indicating an orthorhombic distortion. In the latter case, the peak width stays constant, indicating the absence of a measurable monoclinic distortion. The subscripts t and o denote the use of the tetragonal and orthorhombic unit cells, respectively.

on the dimensionality of the system since it has been observed in the perovskite, the double-layer and the single-layer compounds. In this Sec., we discuss the distortion in the single-layer manganite $\text{La}_{1-x}\text{Sr}_{1+x}\text{MnO}_4$ in the doping region $0.45 \leq x < 0.70$. We first present our results for the commensurate doping $x = 0.50$ and then extend the discussion to other doping levels. Finally, we discuss the magnetic properties of the compounds in this region of the phase diagram.

A. Structural Properties of LaSrMnO_4 ($x = 0.50$)

$\text{La}_{0.50}\text{Sr}_{1.50}\text{MnO}_4$ undergoes a structural phase transition at approximately 230 K. The low-temperature phase is characterized by superlattice reflections with wavevector $(\frac{1}{4}, \frac{1}{4}, 0)_t$.^{4,5,8,12} The symmetry of the lattice can be established from extinction rules and high-resolution powder diffraction analysis. Powder diffractometry is a very reliable and sensitive probe of small lattice distortions because peaks corresponding to an identical d -spacing merge irrespective of the angular orientation, and hence very small changes in the d spacing are readily visible. At room temperature, the powder diffraction peaks of $\text{La}_{0.50}\text{Sr}_{1.50}\text{MnO}_4$ can be indexed on a tetragonal lattice with lattice parameters $a_t \approx 3.86$ Å and $c_t \approx 12.42$ Å. However, as demonstrated in Fig. 9, below the transition temperature, the $(2, 2, 0)_t$ peak splits into two, but the $(2, 0, 0)_t$ peak does not split or broaden. This indicates that the lattice becomes orthorhombic with a 45°

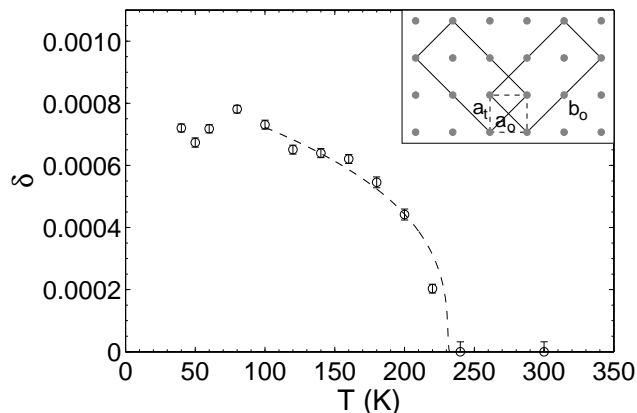


FIG. 10: Orthorhombicity $\delta = |1 - b_o/(2a_o)|$ as function of temperature for $\text{La}_{0.50}\text{Sr}_{1.50}\text{MnO}_4$. The structural transition occurs at $T_{COO} = 231.5(5)$ K, as determined from the temperature dependence of a superstructure peak (Fig. 14). The dashed curve is a guide to the eye. Inset: Structural unit cells (a - b plane) for $x = \frac{1}{2}$. The tetragonal high-temperature (orthorhombic low-temperature) unit cell is shown by dashed (continuous) lines. At low temperature, there exist two twin domains that are rotated by 90° with respect to each other. Only the manganese sites are shown.

rotation of the axes in the a - b plane (a broadening of the $(h,0,0)_t$ type reflections would indicate a further monoclinic distortion). The orthorhombicity varies as function of the temperature, as shown in Fig. 10. The low-temperature and high-temperature unit cells are illustrated in the inset of Fig. 10.

The symmetry of the low-temperature phase for $x = 1/2$ was investigated further through a thorough survey of the reciprocal space of a single crystal. The reciprocal space map shown in Fig. 11 exhibits the extinction symmetry $B---$. A particularity of the low-temperature structure is the weakness of the reflections with $H_o = 0$ and K_o odd. These reflections are two to three orders of magnitude smaller than equivalent reflections with H_o different from zero. This suggests that the crystal has a pseudo-symmetry b -glide and should thus be a subgroup of the $Bm\bar{m}$ space group. $B2mm$ is the sole orthorhombic space group with the proper extinction symmetry, and is thus the most probable space group. A schematic of the distortion with the space-group symmetry $Bbmm$ is shown in Fig. 12.

Because of severe x-ray absorption and extinction effects, we were not able to accurately determine the structure factors for the reflections, and hence were unable to calculate the atomic displacements to further establish the nature of the distortion. Nevertheless, a few characteristics of the partially-determined structure are worth pointing out. A first characteristic is the presence of a mirror plane within the Mn-O layer, perpendicular to $[0,0,1]$. Its presence forbids any buckling of the Mn-O plane. Second, as a result of the low $B2mm$ symmetry,

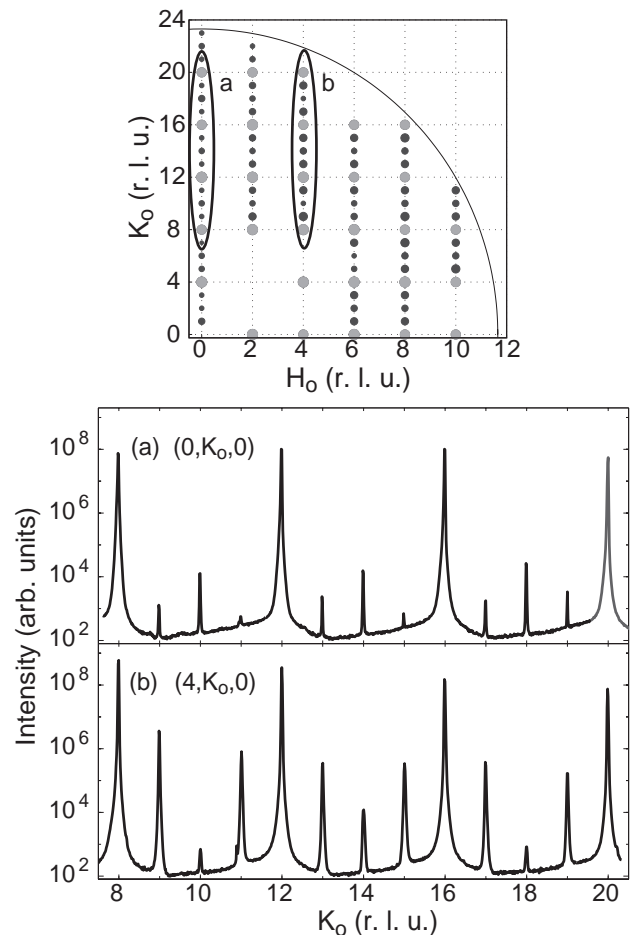


FIG. 11: (Top) Intensity map of the Bragg reflections in the $L = 0$ plane at 100 K for $\text{La}_{0.50}\text{Sr}_{1.50}\text{MnO}_4$. The gray circles represent the high-symmetry Bragg peaks of the $I4/m\bar{m}$ structure, and the black circles represent the additional superlattice Bragg peaks of the low-temperature phase. The radius of the circles is proportional to the logarithm of the intensities. The reciprocal lattice corresponds to the low-temperature orthorhombic cell with $a_o = 5.46$ Å, $b_o = 10.92$ Å, and $c_o = 12.4$ Å. The line (quarter circle) represents the maximum reachable momentum at the x-ray energy of 14 keV used in our experiment. Several reflections, for example $(2, 1, 0)_o$, could not be reached due to geometric constraints. This map should be considered qualitative since absorption and extinction are considerable in this material for 14 keV x-rays. (Bottom) Two specific scans are shown, corresponding to the two regions labeled (a) and (b) on the map.

there exist three distinct manganese sites with a ratio of manganese atoms of 2:1:1. The single-multiplicity Mn sites are related by the pseudo-glide plane. Finally, the inclusion of the pseudo-glide plane in the set of symmetry operators generates the supergroup $Bbmm$, in which the lattice distortion resulting in the low-temperature structure is a shear-type distortion rather than a breathing-type distortion. A breathing-type distortion would have a mirror plane perpendicular to $[1,0,0]_o$ and would have

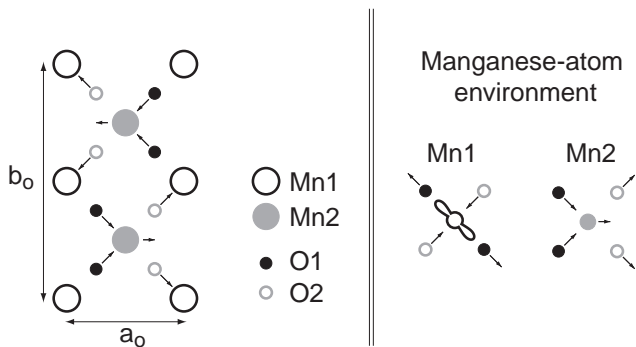


FIG. 12: Low-temperature distortion of the Mn-O plane with space-group symmetry $Bbmm$. There are two manganese sites and two basal oxygen sites in this space group. The Mn1 (Mn2) sites are occupied by “Mn³⁺” (“Mn⁴⁺”) ions. The panel on the right shows the distortion around each type of Mn site. The actual $B2mm$ symmetry of $\text{La}_{0.5}\text{Sr}_{1.5}\text{MnO}_4$ is lower than that indicated here, with three rather than two inequivalent manganese sites, as discussed in the text.

$Bmmm$ symmetry.

The symmetry proposed here for the low-temperature phase of $\text{La}_{0.5}\text{Sr}_{1.5}\text{MnO}_4$ is in good agreement with previous electron diffraction results,^{4,5} but it is lower than that reported in Ref. 7 based on neutron scattering measurements. We confirmed, through neutron scattering measurements, that the Bragg reflections with wavevector $(\frac{1}{4}, \frac{1}{4}, 0)_t$ result from the bulk of the sample, and thus our neutron scattering data are in good agreement with our x-ray results. Finally, the symmetry identified by Raman scattering is $Pbmm$.²⁸ This is a subgroup of the pseudo-symmetry identified here ($Bbmm$) which differs only in the centering of the lattice (primitive versus face centered). The symmetry of the atomic sites in both space groups is the same. Consequently, both have the same Raman active modes. Therefore, $Bbmm$ is an acceptable symmetry to model the Raman modes. The breaking of the symmetry from $Bbmm$ to $B2mm$ is probably too weak to be observable as additional Raman modes.

Based on a local density of states calculation, it was concluded²² that the symmetry of the lattice structure is $Bbmm$, the pseudo-symmetry obtained experimentally. The calculation established that half of the manganese sites have a Jahn-Teller-type elongation of the surrounding oxygen octahedron (the so-called “Mn³⁺” sites) while the octahedra around the other sites are much less distorted (“Mn⁴⁺” sites). Furthermore, it was concluded that the difference in valence between the two sites should be relatively small. Unfortunately, the present scattering analysis can not solve this issue since the determination of the Mn valences requires the knowledge of the Mn-O bond distances (bond valence sum). A major difference between the crystal structures derived from the LDA calculation (space group $Bbmm$) and from experiments ($B2mm$) is that, in the former, there are only two unique manganese sites, while in the latter, there are three. In both structures, there is only one “Mn³⁺” site. How-

ever, our diffraction measurements imply the existence of two crystallographically distinct “Mn⁴⁺” sites. From our measurements (from the strengths of the $(h, 0, 0)_o$ reflections), we conclude that the difference between the two “Mn⁴⁺” sites is small.

The mostly shear-type distortion of the planar oxygen sublattice in the $Bbmm$ structural model makes the resonant terms of the x-ray scattering tensor around the Mn sites highly anisotropic, as shown in Ref. 22, for example. The magnitude and the symmetry of the calculated anisotropy is in complete agreement with previous resonant scattering measurements,⁸ again confirming the validity of the proposed symmetry for the low-temperature phase of $\text{La}_{0.5}\text{Sr}_{1.5}\text{MnO}_4$.

A number of perovskites and double-layer manganites at or near $x = 0.50$ have closely related low-temperature phases. Structural refinements based on neutron and x-ray powder scattering as well as single-crystal neutron scattering are available for several compounds: $\text{La}_{0.5}\text{Ca}_{0.5}\text{MnO}_3$,⁶¹ $\text{Nd}_{0.5}\text{Sr}_{0.5}\text{MnO}_3$,⁶² $\text{LaSr}_2\text{Mn}_2\text{O}_7$,⁶³ and $\text{Pr}_{0.6}\text{Ca}_{0.4}\text{MnO}_3$.⁶⁴ Consistent with our observations for $\text{La}_{0.5}\text{Sr}_{1.5}\text{MnO}_4$, all these materials were found to have a unit cell with a - b plane dimensions $\sim \sqrt{2}a_t \times 2\sqrt{2}a_t$, with a_t the NN Mn-Mn distance. Three of the structures also share the basic feature that half the manganese sites exhibit a strong Jahn-Teller-type distortion while the oxygen octahedra surrounding the other manganese sites are nearly undistorted. The structure of the fourth compound, $\text{Pr}_{0.6}\text{Ca}_{0.4}\text{MnO}_3$, has been argued to be quite different,⁶⁴ with manganese sites that all have equivalent short and long Mn-O bonds, and a distortion due to a formation of molecular units of Mn-O-Mn. However, recent resonant x-ray diffraction work is consistent with inequivalent Mn atoms that order in a CE-type pattern.⁶⁵ Therefore, at least three of the above four $n = 2$ and $n = \infty$ compounds have distortions that are compatible with the $B2mm$ symmetry proposed here for the low-temperature structure of $\text{La}_{0.5}\text{Sr}_{1.5}\text{MnO}_4$.

Based on bond valence sums, the difference between the crystallographically distinct Mn ions in $\text{Pr}_{0.6}\text{Ca}_{0.4}\text{MnO}_3$ is insignificant.⁶⁴ On the other hand, bond valence sums for the other three compounds show some degree of charge disproportionation between the two manganese sites: 3.5 and 3.9 for $\text{La}_{0.5}\text{Ca}_{0.5}\text{MnO}_3$,⁶¹ 3.49 and 3.98 for $\text{Nd}_{0.5}\text{Sr}_{0.5}\text{MnO}_3$,⁶² 3.67 and 3.87 for $\text{LaSr}_2\text{Mn}_2\text{O}_7$.⁶³ $\text{La}_{0.5}\text{Sr}_{1.5}\text{MnO}_4$ has a similar low-temperature structural distortion and, thus, it is probable that it also exhibits some degree of charge disproportionation, although with a magnitude that can be expected to be significantly less than a whole electron. As discussed below, charge disproportionation on the Mn sites in the single-layer compounds might help explain the experimental results obtained for $x > 0.50$.

We also investigated the temperature dependence of the superlattice reflections. Below the transition temperature, the superlattice peak $(9, 0, 0)_o$ was scanned along the three principal orthogonal axes and the integrated intensity was obtained by modeling the profiles

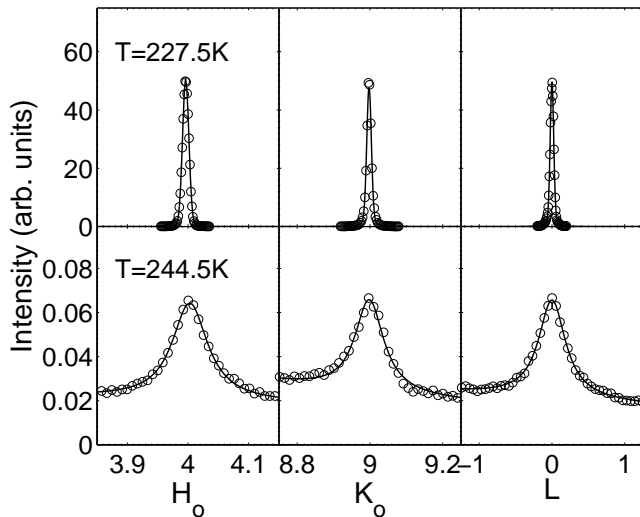


FIG. 13: Representative H_o , K_o and L scans of the $(9, 0, 0)_o$ superlattice peak of $\text{La}_{0.5}\text{Sr}_{1.5}\text{MnO}_4$. The upper (lower) panels show scans below (above) the Néel temperature.

with pseudo-Voigt functions. Representative scans are shown in the top panels of Fig. 13 and the integrated intensity is displayed in Fig. 14. Near the transition temperature, the data exhibit a rounding of about 3 K, which was too large to allow a meaningful critical scattering analysis. Heat capacity measurements on a piece from the same crystal boule also showed broadening, in this case of about 4 K. The broadening is most likely due to La/Sr inhomogeneities. The transition is probably second order, since we found no signs of hysteresis, and because there exist large fluctuations with continuously varying correlation lengths above the charge/orbital ordering temperature $T_{COO} = 231.5(5)$ K.

In the ordered phase of $\text{La}_{0.5}\text{Sr}_{1.5}\text{MnO}_4$, the peak widths along $[1, 0, 0]_o$ and $[0, 1, 0]_o$ increased continuously as the temperature was lowered while it remained constant along $[0, 0, 1]_o$. This increase is associated with an increase of the crystal mosaic as the lattice becomes increasingly more orthorhombic and, hence, more strained (the correlation between the mosaic and the $[1, 0, 0]_o$ and $[0, 1, 0]_o$ directions resulted from the scattering geometry of the experiment). The widths of the superlattice reflections in all three directions were broader than those of the high-symmetry peaks, with correlations of about 200 Å along $[0, 0, 1]_o$ and at least 1000 Å along $[1, 0, 0]_o$ and $[0, 1, 0]_o$.

Above the transition, the superlattice peaks broadened considerably. The bottom panels of Fig. 13 show representative scans along the three principal orthorhombic directions at $T = 244.5$ K. The scattering intensity was modeled as a convolution of the correlation function and the resolution function. An effective resolution function was defined from the peak shape of a nearby high-symmetry peak, $(4, 8, 0)_o$, at a temperature of 232 K,

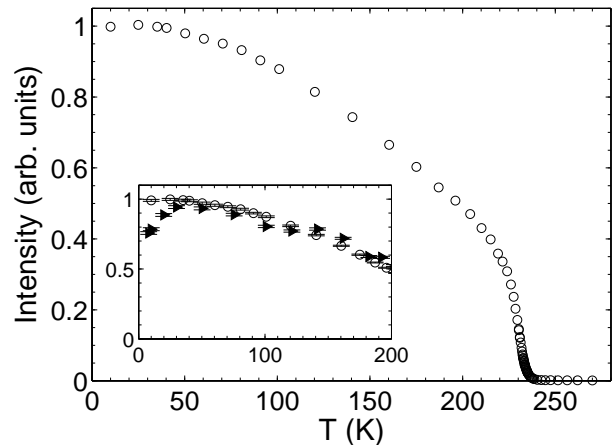


FIG. 14: Linear plot of the $(4, 9, 0)_o$ Bragg peak intensity in the ordered phase for $x = 0.50$ as function of the temperature. The transition temperature is found to be $231.5(5)$ K. Inset: Integrated intensity of the $(4, 9, 0)_o$ superlattice reflection for two different levels of x-ray flux on the sample. The high flux level is ~ 300 times larger than the low flux. A partial melting of the ordered phase can be observed at low temperature for the data collected with the higher flux (black triangles).

just above T_{COO} . A pseudo-Voigt form was fitted in all three directions. Consequently, this resolution function included the crystal mosaicity in addition to the fundamental instrumental resolution. The correlation function used was a Lorentzian:

$$C(\mathbf{q}) = \frac{C(0)\kappa^2}{\kappa^2 - (\mathbf{q} - \mathbf{G})^2} \quad (7)$$

where $C(0)$ is the amplitude, \mathbf{G} is the position of the Bragg peak, and κ is the inverse correlation length.

Measurements in the high-temperature phase indicate that the structural correlations are very anisotropic. Figure 15 reveals that the in-plane correlations are nearly isotropic, with a ratio $\xi_H/\xi_K \approx 0.63$, while the out-of-plane correlations are much shorter. Above 255 K, the short-range order can be considered two-dimensional, since the out-of-plane correlation length is on the order of the interplane distance, 6.2 \AA ($\approx c_t/2$). The correlation lengths along the H_o and K_o directions cease to decrease above that temperature and are about 20 Å and 13 Å, respectively.

Even though ξ_L remains finite in the ordered phase, the underlying transition appears to be three-dimensional, and not two-dimensional, since the correlation lengths for the three directions (H_o , K_o and L_o) are approximately proportional to each other. The situation in two-dimensional systems, for example the antiferromagnets K_2NiF_4 (Ref. 43) or LaSrMnO_4 (Sec. III), is very different since only two-dimensional fluctuations, that is, two-dimensional scattering rods, are observed. It is difficult to establish the correlation lengths close to the transition, in part because of the chemical inhomogeneities

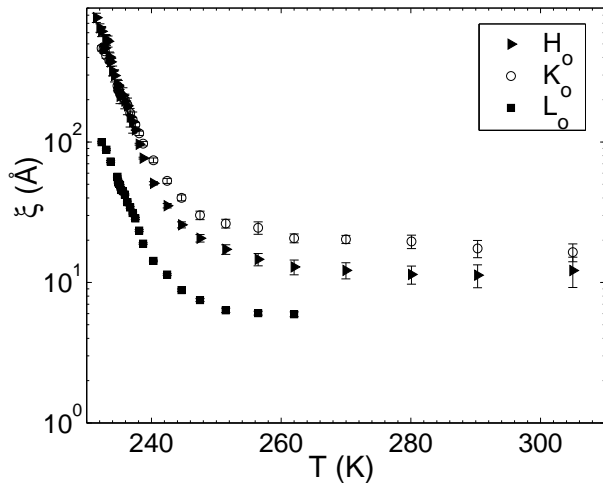


FIG. 15: Logarithmic plot of the correlation length of the charge/orbital order as a function of temperature for $x = 0.50$. Short-range distortions associated with the low-temperature phase are still present at room temperature. The correlation length is nearly constant far above the transition temperature ($T_{\text{COO}} = 231.5(5)$ K).

discussed above, but also because the estimate strongly depends on the shape of the resolution function. The development of full three-dimensional long-range order might be hindered due to the presence of structural defects. We note that it has been suggested that the three-dimensional nature of the charge/orbital order transition in $\text{La}_{0.5}\text{Sr}_{1.5}\text{MnO}_4$ results from an instability toward a structural distortion.⁶⁶

To complete this discussion of the charge/orbital order for $x = \frac{1}{2}$, we present our findings for the effect of the x-ray probe on the charge-ordered phase. At low temperatures, deep in the ordered phase, the scattering intensity at the superlattice position decreases but eventually levels off to a non-zero value when a relatively high x-ray flux is incident on the sample (about 10^{12} photons/second). This partial melting of the ordered phase is demonstrated in the inset of Fig. 14. No such effect was observed when the incident flux was decreased by a factor of 300. A similar partial reduction of the superlattice intensity was found for most dopings in the charge/orbital ordered phase, and it resembles previous results observed for $\text{Pr}_{0.70}\text{Ca}_{0.30}\text{MnO}_3$ (Ref. 34) and $\text{La}_{0.875}\text{Sr}_{0.125}\text{MnO}_3$ (Ref. 35). This effect is likely related to the “melting” of the charge order observed for both $\text{Pr}_{0.70}\text{Ca}_{0.30}\text{MnO}_3$ ⁶⁷ and $\text{La}_{1.5}\text{Sr}_{0.5}\text{MnO}_4$ ³³ when samples were exposed to high-intensity visible light. These observations demonstrate that the low-temperature charge-ordered phase of $\text{La}_{1-x}\text{Sr}_{1+x}\text{MnO}_4$ is unstable when the material is exposed to intense electromagnetic radiation.

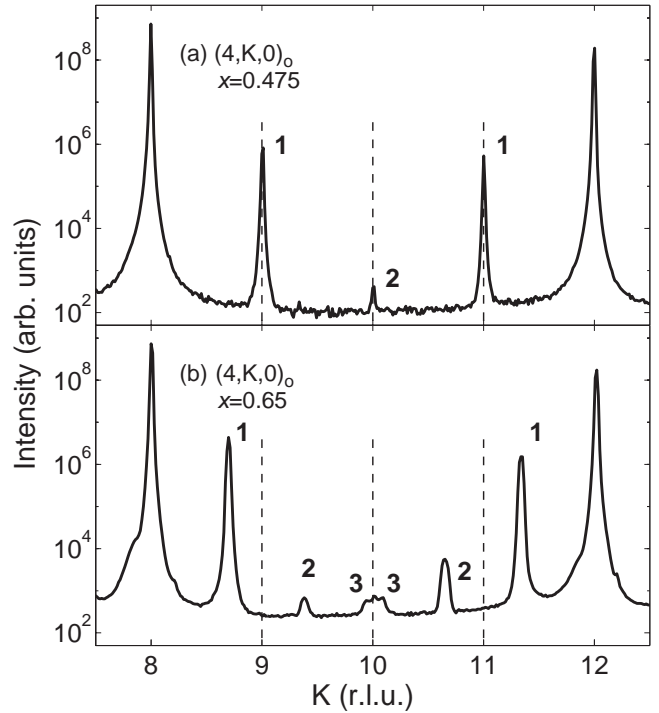


FIG. 16: X-ray diffraction scans of $\text{La}_{1-x}\text{Sr}_{1+x}\text{MnO}_4$ in the low-temperature phase ($T = 7$ K) along $(4, K, 0)_o$ for (a) $x = 0.475$ and (b) $x = 0.65$. The vertical dashed lines indicate the commensurate positions. 1, 2 and 3 label, respectively, the first, second and third harmonics of the low-temperature distortion. Note the logarithmic intensity scale.

B. Structural Properties for $0.45 \leq x < 0.70$

We observed superlattice peaks in all samples with $x > 0.45$, up to $x = 0.67$, the most Sr-rich sample we were able to grow as a single crystal. Figure 16 compares results for $x = 0.475$ and $x = 0.65$. For $x > 0.50$, the superlattice modulation vector ϵ changes linearly with the e_g electron density $n_e = 1 - x$, as shown in Fig. 17. At $x = 0.50$, the superlattice modulation doubles the high-temperature structure (along the tetragonal base diagonal), and at $x = 0.67$, it triples it. This linear dependence of the wavevector is similar to that observed in $\text{La}_{1-x}\text{Ca}_x\text{MnO}_3$ for $x > 0.5$ ⁶⁸ and, in particular, at $x = 2/3$.^{69,70,71,72} While at $x = 1/2$ and $x = 2/3$ commensurate wavevectors are observed, the order is best understood, at all doping levels $1/2 \leq x \leq 2/3$, as a modulation whose period is a linear function of the doping x . We note that a section of one of our crystals with nominal doping of $x = 0.65$ had an effective doping level of $x \approx 0.69$, as judged from the measured value of $\epsilon \approx 0.62$ (not shown in Fig. 17).

The incommensurability of the modulation is also affected by the oxygen content. To establish this result, we compared the scattering from two pieces of the same crystal boule with a La/Sr ratio of 0.40/1.60. One piece was as grown, essentially quenched from a high temperature

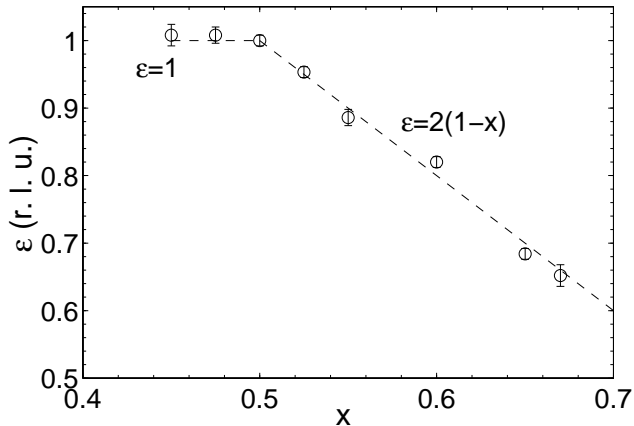


FIG. 17: Parameter ϵ of the low-temperature modulation wavevector $(0, \epsilon, 0)_o$ as function of doping x for $\text{La}_{1-x}\text{Sr}_{1+x}\text{MnO}_4$, determined by synchrotron x-ray diffraction. For $x \geq 0.5$, the value of ϵ is directly related to the e_g electron density $n_e = (1-x)$: $\epsilon = 2n_e$.

in an environment with a relatively high oxygen partial pressure (5 bar). The other sample was annealed for 24 h in a flow of argon with an oxygen partial pressure of 10^{-5} bar at a temperature of 950°C . The second sample had a mass of 148.4 mg and exhibited a mass difference of 0.3(2) mg after the anneal, corresponding to a change in the oxygen content of 0.04(3). Figure 18 demonstrates that the incommensurability (the deviation of the peak position from $K_o = 9$) decreased after the anneal. Using the linear relationship between the incommensurability and the nominal Mn valence established in Fig. 17, one finds that the nominal Mn valence of the as-grown sample is 3.595 while that of the annealed sample is 3.56. In this simple ionic model, this result implies an oxygen content change of approximately 0.02, which is within the uncertainty of the mass measurement. Thus, the period of the modulation can be linked to the e_g electron density n_e . Because the superlattice modulation is directly correlated with n_e , it is likely that the structural phase transition is driven by the ordering of the e_g electrons.

In Fig. 16, second and third diffraction harmonics, much weaker than the primary, are visible at $(0, \pm 2\epsilon, 0)_o$ and $(0, \pm 3\epsilon, 0)_o$. The relative weakness of the higher harmonics suggests that the structural distortion is essentially sinusoidal: a pure sinusoidal modulation is described by a single Fourier component and exhibits weak higher harmonics.⁷³ In contrast, a nonsinusoidal modulation, especially one with sharp discontinuities, would exhibit strong higher harmonics. For example, a square-wave modulation would exhibit strong odd harmonics; the intensity of the third harmonic would be more than 10% of that of the fundamental. Finally, we note that the widths of the superlattice peaks along $[1, 0, 0]_o$ and $[0, 1, 0]_o$ are comparable to those of the high-symmetry peaks, which implies that the low-temperature phase ex-

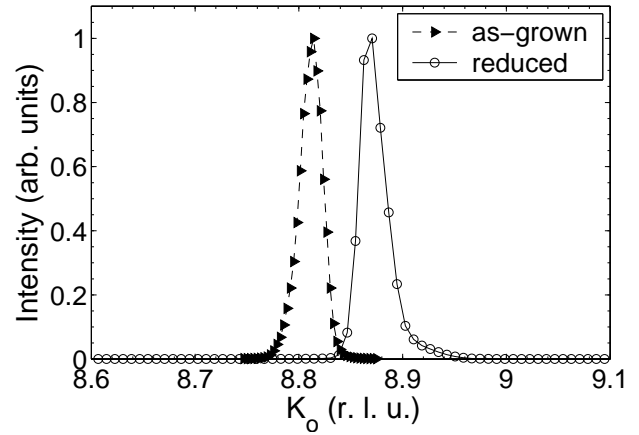


FIG. 18: K_o -scans through the $(4, 8 + \epsilon, 0)_o$ reflection for two samples with the same La/Sr content ($x = 0.60$), but different oxygen stoichiometry. The first sample is as-grown while the second sample was annealed in argon ($P_{O_2} = 10^{-5}$ bar) at 950°C for 24 h.

hibits long-range order parallel to the Mn-O plane.

The nearly sinusoidal structural distortion, together with the linear variation of the modulation wavevector with doping, precludes any model in which the e_g electron order is too closely linked to the underlying cationic lattice, such as the bi-stripe model,⁶⁹ the topological scenario for stripe formation,⁷⁴ or the the discommensurate-stripe model proposed for the single-layer nickelates.⁷⁵ A better description is given by a nearly sinusoidal structural distortion, probably associated with a charge-density wave. The variation of the charge density, with equivalent Mn sites located as far apart as possible, is similar to the “Wigner-crystal” arrangement of the e_g electrons proposed for $\text{La}_{0.333}\text{Ca}_{0.667}\text{MnO}_3$ ⁷⁰ (the term “Wigner-crystal” is somewhat unfortunate since the situation it describes is rather different from the classical Wigner crystal in which the electronic wave functions form a crystal independent of the nuclear lattice, as is observed in some semiconductors).

For $0.45 \leq x < 0.50$, the modulation vector remains the same as for $x = 0.50$. However, the intensity of the superlattice peak increases as x increases toward $x = 0.50$.¹² The simplest explanation for this behavior is that the material separates into charge-ordered regions of 0.5 e_g electrons per Mn site and disordered regions of approximately 0.55 e_g electrons per Mn site. For compositions with $x < 0.45$, $\text{La}_{1-x}\text{Sr}_{1+x}\text{MnO}_4$ only exhibits short-range order. This will be discussed in Sec. V.

C. Magnetic Properties for $0.45 \leq x < 0.70$

Using neutron scattering, we studied the magnetic order of several samples in the composition range $x \geq 0.45$. The doping levels of the samples were 0.475, 0.50, 0.60 and 0.65. The first two samples showed Néel order be-

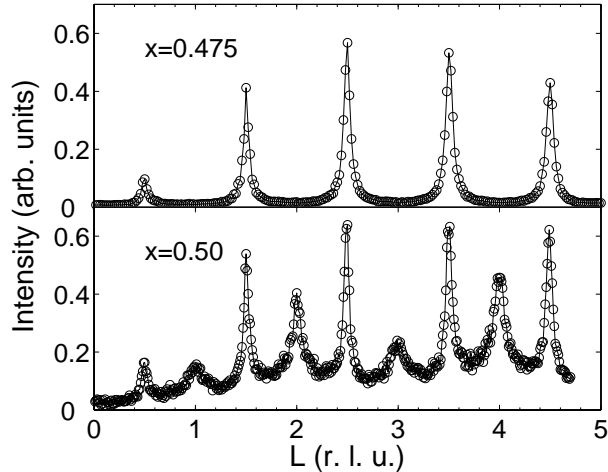


FIG. 19: Neutron diffraction scans along $(1, 0, L)_o$ for $x = 0.475$ and $x = 0.50$. The measurements were taken at 13 K and 7 K, respectively, on the spectrometer BT7 with 13.4 meV neutrons and collimations of 35'-40'-sample-25.8'-open.

low 115 K, while only short-range antiferromagnetic order was observed in the two higher-doped samples. In all cases the magnetic-order wavevector was found to be commensurate with the lattice: $(1, 0, L)_o$.

For the two long-range-ordered samples, the observed magnetic structure is in good agreement with previous results⁷ for $x = 0.50$, and it agrees with the CE structure. The authors of Ref. 7 reported peaks corresponding to two stacking patterns along $[0, 0, 1]$. The majority (minority) stacking pattern has magnetic peaks at half-integer (integer) L positions, corresponding to antiferromagnetic (ferromagnetic) next-NN planes, i.e., planes separated by a distance $c \approx 12.4$ Å. In the $x = 0.475$ sample, we only observed peaks associated with the majority stacking pattern while, for $x = 0.50$, we observed both patterns with a ratio slightly different from that in Ref. 7 (see Fig. 19). The $x = 0.50$ sample also exhibits significant diffuse scattering which gives rise to the higher background level seen in the bottom panel of Fig. 19. Figure 20 demonstrates that the two sets of peaks in this sample have different temperature dependences, with transitions of 105 K (L integer) and 120 K (L non-integer). In both samples, only short-range order was observed along $[0, 0, 1]$, while the peaks were resolution limited in the H - K plane. The correlation lengths are $\xi_c = 60(4)$ Å for the majority stacking pattern (in both samples) and $\xi_c = 30(4)$ Å for the minority stacking pattern ($x = 0.50$ only). The lengths do not vary below the Néel transition.

A power-law with Gaussian broadening (solid line in Fig. 20) gave a good fit of our $x = 0.475$ data above 50 K, with $T_N = 110(1)$ K, $\beta = 0.24(3)$, and a distribution of Néel temperatures with width (FWHM) of 15(1) K. The rounding is remarkably large, nearly an or-

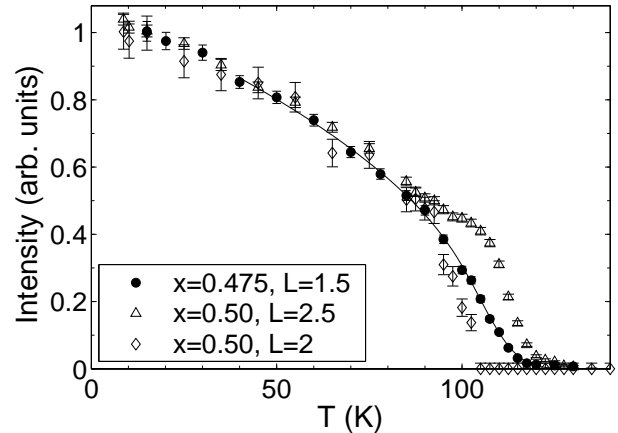


FIG. 20: Magnetic order parameter curves of the antiferromagnetic phase for samples with doping $x = 0.475$ and $x = 0.50$, as described in the text.

der of magnitude larger than that typically found for the structural transition, and significantly larger than for the magnetic transitions in the low-doping regime. One possible explanation for this observation is that, unlike for $x = 0$, the leading magnetic anisotropy is planar rather than uniaxial. It has been argued that realistic, finite-size two-dimensional XY systems (or systems with a leading XY anisotropy) should be characterized by a non-zero magnetization with effective exponent $\beta \approx 0.23$ and a significant effective rounding of the transition.⁷⁶ Therefore, the value $\beta = 0.24(3)$ is consistent with the existence of a significant planar anisotropy.

Above the Néel transition, there exist significant two-dimensional antiferromagnetic correlations for the $x = 0.475$ sample which are observable in the form of scattering rods. The scans shown in Fig. 21 were taken using a two-axis neutron spectrometer configuration in order to integrate over the energy of the fluctuations and to measure the instantaneous spin-spin correlations. The data are more limited than for $x \leq 0.15$ (Sec. III), and we were not able to distinguish between in-plane (along $[1, 0, 0]_o$) and out-of-plane (along $[0, 0, 1]_o$) contributions. The correlation lengths were extracted from the scans by assuming a single isotropic two-dimensional Lorentzian cross section convoluted with the instrument resolution. We note that, due to the geometry of the experiment, the measurement was not very sensitive to the fluctuations along $[0, 1, 0]_o$. Figure 22 compares the correlation lengths for two compositions: $x = 0.475$ and $x = 0.00$. The latter result was discussed in Sec. III. Interestingly, even though these two samples belong to two very different magnetic phases, the high-temperature correlation lengths are indistinguishable. The two compounds thus probably have very similar values of the spin stiffness. We observe no sign of a diverging length for $x = 0.475$ even rather close to the onset of long-range magnetic order.

The discrepancy at low temperature can be explained

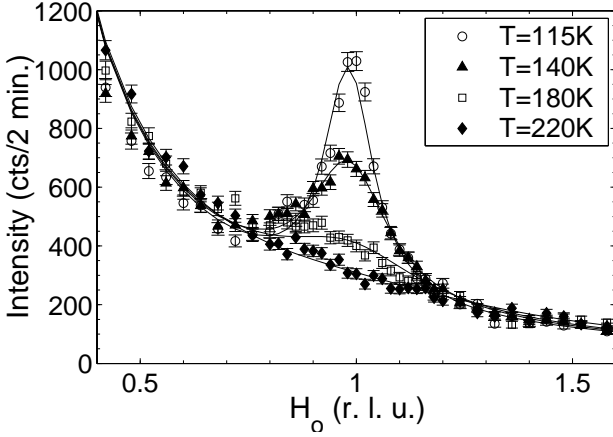


FIG. 21: Energy-integrating scans of the magnetic fluctuations in the disordered phase for $x = 0.475$ (two-axis neutron scattering mode) in the paramagnetic phase. The lines are fits to a two-dimensional isotropic Lorentzian cross section convoluted with the instrument resolution. The data were taken on the spectrometer BT7 with 13.4 meV initial energy neutrons and collimations of 35'-40'-sample-25.8'-open.

by assuming that for $x = 0.475$ there exist anisotropic a - b -plane spin correlations with $\xi_b \gg \xi_a$ and a (possibly small) in-plane Ising anisotropy (in addition to an easy-plane anisotropy), in contrast to the out-of-plane Ising anisotropy for $x = 0.00$. While our data for $x = 0.475$ establish that the magnetic scattering in the paramagnetic phase is two-dimensional, they are not sufficient to conclude whether the nonequivalence of the H_o and K_o axes in the CE magnetic structure causes an anisotropy of the in-plane magnetic correlation lengths; the two-axis scans primarily reflect the correlation in the H_o direction, perpendicular to the ferromagnetic chains of the CE structure, and a two-dimensional isotropic Lorentzian cross section was assumed in the data analysis.

The presence of short-range magnetic correlations between the Néel temperature and the charge/orbital order transition temperature has been argued to be necessary for the stabilization the charge/orbital ordered state. For example, it has been suggested that the correlations must be long along the ferromagnetic chains (along $[0,1,0]_o$) and short in the other directions.⁷⁷ More experimental work is required to test these predictions.

The two higher-doped samples, $x = 0.60$ and $x = 0.65$, only showed short-range magnetic order, essentially uncorrelated along $[0,0,1]$ (the correlation length is less than the interplane distance). Along $[1,0,0]_o$, the peaks occur at the same commensurate positions as for $x = 0.475$ and $x = 0.50$. For both samples, the low-temperature correlation length along $[1,0,0]_o$, determined from triple-axis scans (see Fig. 23), is only 29(1) Å. As demonstrated in Fig. 24, the peak intensity decreases approximately linearly with increasing temperature as the correlations become shorter. We observed a magnetic signal up to about 200 K.

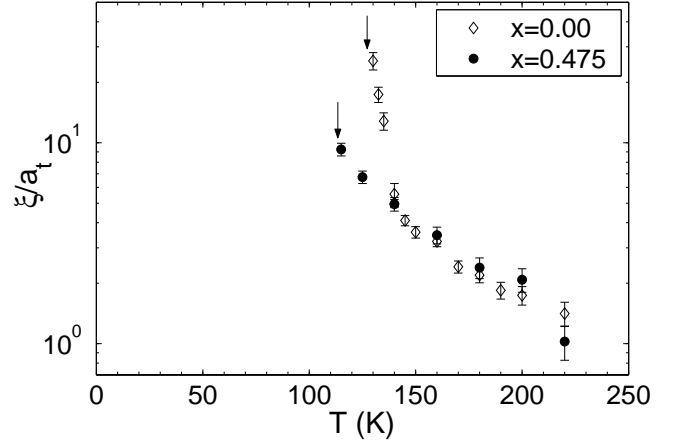


FIG. 22: Instantaneous antiferromagnetic correlation length as function of temperature for $x = 0$ and $x = 0.475$. The downward arrows indicate the onset of long-range magnetic order.

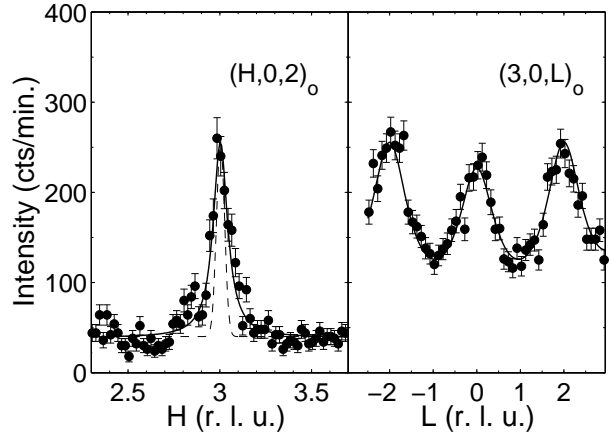


FIG. 23: Triple-axis scans of the short-range magnetic correlations in a $x = 0.60$ sample at low temperature ($T = 9$ K). The dashed line in the left panel represents the instrument resolution. The magnetic correlations are short-range and essentially two-dimensional. The correlation length, as estimated from these triple-axis scans, is about 3.5 Å along $[0,0,1]_o$ and 29(1) Å along $[1,0,0]_o$. The data were taken on the spectrometer BT7 with 13.4 meV neutrons and collimations of 35'-40'-sample-25.8'-open.

We note that the large $x=0.60$ and $x=0.65$ samples used in the neutron scattering measurement were of somewhat lower quality than the small samples used for x-ray scattering and those grown at lower strontium concentrations. The sample mosaics were on the order of one degree. Also, the structural superlattice peaks were broadened along the incommensurability direction, indicating the existence of chemical inhomogeneities of about $\Delta x = 0.03 - 0.04$ (FWHM). However, it is unlikely that a significant second phase with doping $x=0.50$ exists in these $x=0.60$ and $x=0.65$ samples, since no evidence of

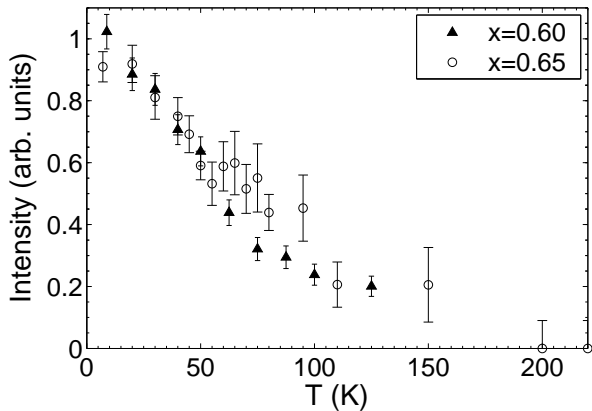


FIG. 24: Temperature dependence of the antiferromagnetic short-range peak intensity in samples with doping $x = 0.60$ and 0.65 .

structural scattering was observed at the commensurate position that could be associated with the commensurate magnetic response.

The magnetic properties in this region of the phase diagram are quite different from those of $\text{La}_{0.33}\text{Ca}_{0.67}\text{MnO}_3$, which has a very similar lattice distortion. The latter exhibits magnetic long-range order, with a wavevector compatible with the tripling of the structural unit cell.⁷⁰ It is thus quite surprising that the magnetic response of $\text{La}_{1-x}\text{Sr}_{1+x}\text{MnO}_4$ is commensurate with the underlying Mn-O lattice and, consequently, incommensurate with the structural distortion. It is probable that any long-range magnetic order would have to be commensurate with the lattice distortion modulation (i.e., incommensurate with the underlying Mn-O lattice), since it is unlikely that magnetic order and charge order are decoupled. We speculate that for $x > 1/2$ long-range magnetic order is forbidden in $\text{La}_{1-x}\text{Sr}_{1+x}\text{MnO}_4$ because of magnetic frustration effects, possibly associated with chemical disorder, and due to the two-dimensional nature of the fluctuations.

V. THE INTERMEDIATE REGION ($0.15 < x < 0.45$)

The long-range superstructure order observed at higher doping disappears rapidly as the doping level x is lowered below $x = 0.45$. In the intermediate doping regime, we find diffuse commensurate scattering that is very similar to that in the disordered high-temperature phase for $x = 0.50$. The peak position is slightly displaced: it is $(0.26, 0.26, 0)_t$ instead of $(\frac{1}{4}, \frac{1}{4}, 0)_t$ for $x = 0.50$. In the $x = 0.50$ sample, both the long-range distortion of the low-temperature phase and the short-range distortion of the room-temperature phase are characterized by the commensurate wavevector $(\frac{1}{4}, \frac{1}{4}, 0)_t$.

The intensity of the diffuse structural scattering de-

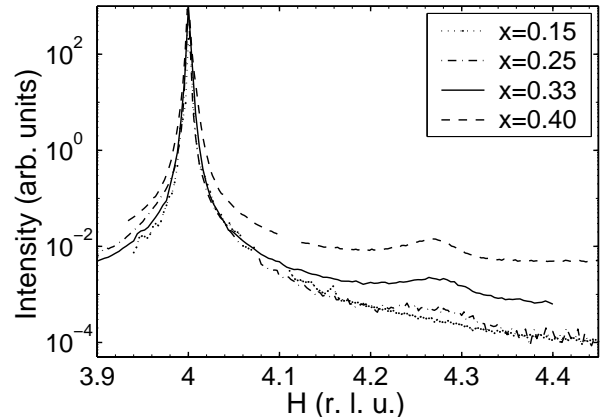


FIG. 25: Scans along $(H, 8 - H, 0)_t$ for $x = 0.40$, $x = 0.33$ and $x = 0.25$ revealing diffuse peaks indicative of short-range order. At lower doping ($x = 0.15$), however, no peak is observable. Small secondary-phase peaks were found at $H = 4.07$ ($x = 0.15$ and $x = 0.25$) and at $H = 4.12$ ($x = 0.40$), but are not included in the figure.

creases rather rapidly at low doping, as can be seen in Fig. 25. The peak intensity decreases by an order of magnitude between $x = 0.40$ and $x = 0.33$ (this comparison should be considered qualitative since absorption and extinction effects are considerable). The diffuse peak is still visible for $x = 0.25$, but not for lower values of doping.

As can be seen in Fig. 26, the temperature dependence of both the intensity and the correlation length is weak. At low temperature, the integrated peak intensity decreases. Since these data were taken with a high x-ray flux, this decrease may be due to partial x-ray induced melting, similar to the effect observed in the long-range charge-ordered compounds (see Fig. 14). The size of the correlated regions is comparable to those for $x = 0.50$ in the disordered high-temperature phase (see Fig. 15). The onset temperature of the observed signal is about 250 K.

Besides the diffuse scattering at the superlattice positions, significant diffuse intensity was also observed in the “tails” of the Bragg peaks, as can be seen from Fig. 27. We believe that the majority of this diffuse intensity results from Huang scattering due to point defects, which can be calculated by modeling the local distortion of the lattice due to these defects.⁷⁸ Thermal vibrations distort a crystalline lattice, and these distortions of the perfect lattice lead to a transfer of some of the scattering intensity from the Bragg peaks to their tails. The diffuse intensity in the tails due to thermal vibrations is commonly referred to as thermal diffuse scattering (TDS). A detailed analysis of the temperature dependence of the diffuse intensity in the tails of the Bragg peaks of compounds with $0.25 < x < 0.45$ reveals an additional contribution. At temperatures much higher than those corresponding to the energy of the acoustic phonons in the momentum range of the measurement (essentially the

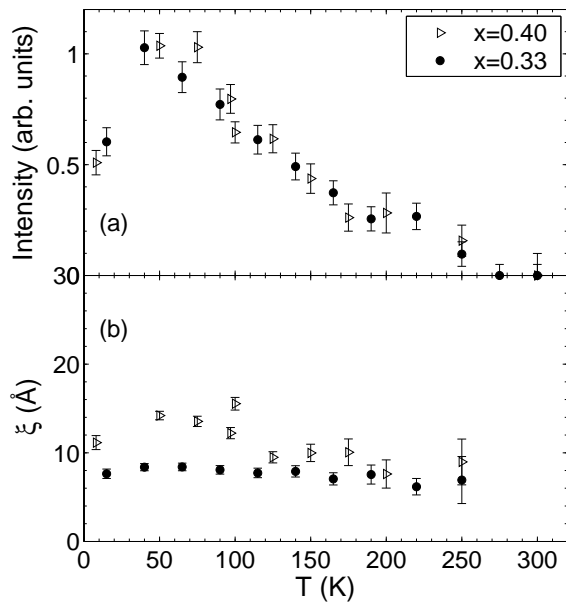


FIG. 26: (a) Integrated intensity and (b) correlation length along $[1,0,0]_o$ of the structural short-range order peaks as function of temperature for two samples with intermediate doping: $x = 0.33$ and $x = 0.40$.

whole temperature range of the measurements reported here), a simplification of the Bose factor that controls the phonon population yields a linear temperature dependence of TDS. As shown in Fig. 28, the subtraction of a linear TDS contribution indeed reveals additional diffuse scattering with an unusual temperature dependence. It can be seen from the bottom panel of Fig. 28 that the non-TDS part of the diffuse scattering scales linearly with the intensity of the correlated peak, and it should thus be related to these short-range distortions. Similar behavior has been found in colossal magnetoresistive double-layer and perovskite manganites.^{79,80,81} In these materials, short-range-ordered peaks and diffuse scattering around the Bragg points were observed to develop in the paramagnetic insulating phase and the resulting distortions were named “polarons.” These should not be seen as classical polarons, and we will refer to them here as correlated “nanopatches.”

However, while the resistivity in the CMR materials correlates well with the scattering strength due to these nanopatches in the paramagnetic insulating phase, the resistivity of the single-layer manganite at these intermediate doping levels is dominated by other factors. The derivative $d\ln(\rho)/dT^{-1}$ is constant in the case of $\text{La}_{1-x}\text{Sr}_{1+x}\text{MnO}_4$,⁵ which indicates that the resistivity ρ is thermally activated. The conductivity is thus polaron-induced (the term polaron is used here with its usual meaning in condensed matter physics). In contrast, the scattering strength of the correlated nanopatches varies much more slowly with temperature, and the resistivity

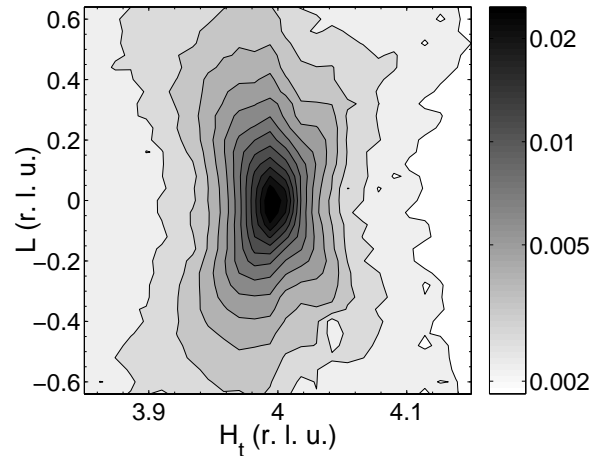


FIG. 27: Logarithmic contour plot of the scattering intensity around the $(4, 4, 0)_t$ peak in a $x = 0.33$ sample. The diffuse scattering is composed of thermal diffuse scattering (TDS) and Huang-like scattering due to Jahn-Teller distortions.

due to the nanopatches varies almost linearly with temperature. Therefore, the nanopatches should not dramatically affect the transport properties of a polaronic insulator, as their contribution to the overall resistivity is minor. In contrast, the situation is very different in a material in which these correlated nanopatches dominate the resistivity, such as the CMR compounds. In these materials, a significant change in the density of these nanopatches, either via changes in temperature or applied magnetic field, dramatically changes the electrical conductivity from metallic to insulating.

A comparison of the short-range distortions of the single-layer ($n = 1$), double-layer ($n = 2$)^{79,82} and perovskite ($n = \infty$)^{80,81} manganites reveals an interesting fact: while all of them share a common CE-type distortion characterized by the wavevector $(\epsilon, \epsilon, 0)_t$, the double-layer manganite also exhibits a distortion with a wavevector of $(\epsilon, 0, 1)_t$, parallel to the Mn-O bond direction.

We also investigated the magnetic properties in this intermediate region of the phase diagram. As described in Sec. III, compounds above the $x_c \approx 0.115$ antiferromagnetic phase boundary exhibit short-range antiferromagnetic correlations (doping levels $x = 0.125$ and $x = 0.15$). In addition, neutron scattering for $x = 0.25$ reveals only very weak two-dimensional scattering rods at wavevector $(1, 0, L)_m$ (i.e., $(\frac{1}{2}, \frac{1}{2}, L)_t$) due to residual short-range correlations of the antiferromagnetic phase at low doping. No correlated antiferromagnetic scattering was observed for $x = 0.40$. Thus, we were unable to detect any CE-type antiferromagnetic correlations in the intermediate doping region.

Given the presence of a ferromagnetic phase in this doping range in the perovskite manganites, we also searched for short-range two-dimensional ferromagnetic correlations. Ferromagnetic correlations are significantly harder to detect than antiferromagnetic correlations,

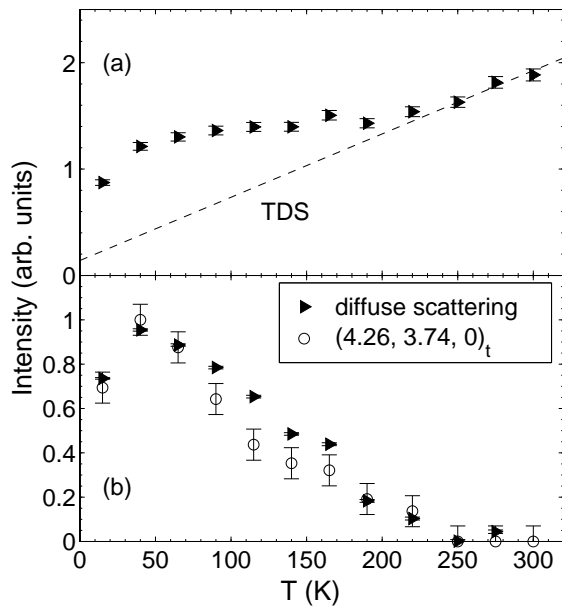


FIG. 28: (a) Linear plot of the diffuse scattering intensity around the $(4, 4, 0)_t$ peak as function of the temperature (for $x = 0.33$). The straight line is an estimate of the thermal diffuse scattering. (b) The Jahn-Teller component of the diffuse scattering near $(4, 4, 0)_t$ scales linearly with the intensity of the broad peak at position $(4.26, 3.74, 0)_t$ shown in Fig. 26a.

because ferromagnetic scattering occurs at the same wavevectors as the structural scattering. Furthermore, there exists a significant amount of diffuse scattering originating from the Bragg reflections along $[0, 0, 1]$ because of the existence of stacking faults in layered compounds. Near $(2, 0, L)_m$, we observed a weak neutron scattering signal that decreased with increasing temperature in the $x = 0.15$ and $x = 0.40$ compounds. This signal most likely originates from the Huang-like structural diffuse scattering discussed above. Thus, we were unable to establish the presence of any ferromagnetic correlations in this part of the phase diagram of $\text{La}_{1-x}\text{Sr}_{1+x}\text{MnO}_4$.

VI. PHASE DIAGRAM AND DISCUSSION

The x-ray and neutron scattering data presented in this paper, together with previously published results, allow the construction of the magnetic and structural phase diagram for the single-layer manganite $\text{La}_{1-x}\text{Sr}_{1+x}\text{MnO}_4$, shown in Fig. 29. As seen in Sec. V, superstructural order exists above $x = 0.45$, with a modulation wavevector that becomes incommensurate for $x > 0.50$. The region $0.45 \leq x < 0.50$ likely is a mixture of the ordered ($x = 0.50$) and disordered ($x \approx 0.45$) structural phases. With the exception of the end compound Sr_2MnO_4 ($x = 1$), the region with doping x above 0.7 has not been stud-

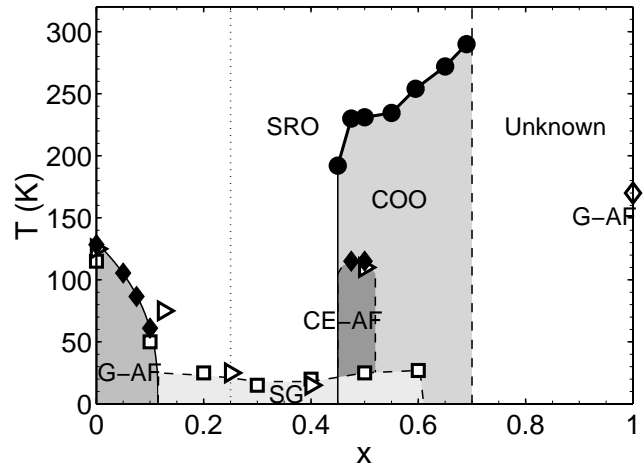


FIG. 29: Magnetic and structural phase diagram of $\text{La}_{1-x}\text{Sr}_{1+x}\text{MnO}_4$. The data come from x-ray structural scattering (\bullet), neutron scattering (\blacklozenge (this work) and \diamond (Ref. 37)), magnetometry (\square , Ref. 4) and muon spin rotation (\triangleright , Ref. 36) measurements. The abbreviations are G-AF: G-type antiferromagnet, CE-AF: CE-type antiferromagnet, SG: spin glass, COO: charge/orbital order phase, SRO: short-range charge and orbital order. The dotted line at $x = 0.25$ does not denote a phase transition, but rather indicates the extent to which SRO is visible. The dashed line at $x = 0.70$ indicates the approximate solubility limit of $\text{La}_{1-x}\text{Sr}_{1+x}\text{MnO}_4$.

ied since powders prepared by the solid state reaction method show two chemical phases⁵ and single crystals could not be successfully grown. The lanthanum-rich part of the phase diagram is not presented here, but the successful preparation of $\text{La}_{1.2}\text{Sr}_{0.8}\text{MnO}_4$ ($x = -0.2$) has been reported.⁸³

Although the temperature dependence of the (anisotropic) superstructure correlations in the high-temperature phase of $\text{La}_{0.50}\text{Sr}_{1.50}\text{MnO}_4$ indicate that the underlying transition is three-dimensional, the correlation length perpendicular to the MnO_2 planes remains finite (~ 200 Å) in the ordered phase, presumably due to the presence of defects. The low-temperature structural symmetry ($B2mm$) is consistent with a Jahn-Teller-type distortion due to orbital ordering. At room temperature for $x \geq 0.45$, and at all temperatures in the range $0.25 \leq x < 0.45$, there exist only anisotropic short-range-distortions. These distortions are quite similar to those observed in the paramagnetic insulating phase of the bilayer and perovskite CMR manganites. However, the resistivities of the single-layer manganite and of the CMR materials differ significantly. While the correlated distortions (“nanopatches”) dominate the transport properties in the latter, the former is a conventional polaronic (or thermally-activated) insulator.

At doping $x > 0.50$, long-range superstructural order similar to that at $x = 0.50$ is present, consistent with a nearly sinusoidal distortion. However, this order is in-

commensurate with the lattice. The incommensurability is affected by both the lanthanum/strontium ratio and the oxygen content. For the as-grown samples studied here, we find the simple relationship $\epsilon = 2(1 - x) = 2n_e$, linking the incommensurability to the e_g electron density $n_e = (1 - x)$. These findings preclude models in which the e_g electron order is too closely linked to the underlying cationic lattice, such as the bi-stripe model,⁶⁹ the topological scenario for stripe formation,⁷⁴ or the discommensurate-stripe model proposed for the single-layer nickelates.⁷⁵

Long-range magnetic order is present in only narrow ranges of doping, near $x = 0$ and $x = 0.5$, and at $x = 1$. In contrast to the structural modulation, the magnetic correlations remain commensurate with the Mn-O lattice at all doping levels. Short-range magnetic correlations, a remnant of the long-range commensurate magnetic order at $x < 0.12$, are visible up to $x \approx 0.25$. A spin-glass phase might exist in this intermediate range, as indicated by magnetometry⁴ and muon-spin-rotation³⁶ measurements, in agreement with the idea of a frustration-induced disappearance of the long-range antiferromagnetic order due to the random distribution of in-plane and out-of-plane Jahn-Teller orbitals.

Comparing the results for $\text{La}_{1-x}\text{Sr}_{1+x}\text{MnO}_4$ with those of the perovskite and double-layer manganites,^{2,3} we conclude that the system with the most similar phase diagram is $\text{La}_{1-x}\text{Ca}_x\text{MnO}_3$.⁸⁴ The phase near $x = 0.50$ is shared by both compounds, with similar patterns of Jahn-Teller distortions and in-plane magnetic structures. Also, in both cases the phase extends to high values of x , and it exhibits similar incommensurate superstructures.⁶⁸ Both compounds are antiferromagnets near $x = 0$, although $(\text{La,Ca})\text{MnO}_3$ is an A-type antiferromagnet while the spin order of $(\text{La,Sr})_2\text{MnO}_4$ is closer to that of the C- and G-type perovskite magnetic structure. The Jahn-Teller distortion around the Mn atoms is also different in the two systems,⁸⁵ as one would expect, considering the strong spin/orbital coupling in the manganites.¹ In the intermediate doping region $0.17 \leq x < 0.50$, $(\text{La,Ca})\text{MnO}_3$ and $(\text{La,Sr})_2\text{MnO}_4$ are both paramagnetic insulators at high temperature with short-range-correlated structural distortions.⁸¹ However, while the former becomes a ferromagnetic metal at low temperature, the latter remains a paramagnetic insulator with very short two-dimensional magnetic correlations. This difference results in the absence of CMR for the single-layer manganite. We believe that the lack of a ferromagnetic phase in $\text{La}_{1-x}\text{Sr}_{1+x}\text{MnO}_4$ is the result of its quasi-two-dimensional structure and the very weak magnetic coupling along $[0,0,1]$.

The single-layer manganite $\text{La}_{1-x}\text{Sr}_{1+x}\text{MnO}_4$ has

three long-range-ordered low-temperature phases at dopings of $x = 0$, $x = 0.50$ and $x = 1$. The two compounds with integer nominal manganese valences, i.e., Sr_2MnO_4 with Mn^{4+} and LaSrMnO_4 with Mn^{3+} , exhibit long-range G-type antiferromagnetic order with an Ising anisotropy and magnetic moments along $[0,0,1]$. The $x = 0.50$ compound shows CE-type spin order with the moments aligned within the $a - b$ plane; it is thus very different from the two end compounds. The phase diagram can be understood by considering the magnetic interactions between manganese sites with formal valences of $3+$ and $4+$. The introduction of Mn^{4+} sites into the Mn^{3+} matrix of LaSrMnO_4 first frustrates the antiferromagnetic order by randomly introducing NN ferromagnetic interactions between Mn^{3+} and Mn^{4+} sites. Near $x = 0.25$, small correlated nanopatches with ordered Mn^{3+} and Mn^{4+} sites appear. A phase transition to large clusters of this mixed-valence order only occurs for $x \sim 0.45$. However, this state is never fully long-range ordered structurally or magnetically perpendicular to the Mn-O planes. Above $x = 0.50$, the persistence of structural order likely indicates that the Jahn-Teller distorted Mn^{3+} sites form a relatively well-ordered pattern, with a modulation wavevector that increases linearly with doping. Finally, at $x = 1$, antiferromagnetic interactions between nearest neighbor Mn^{4+} sites result in a long-range antiferromagnetic state.

In summary, we have carried out a detailed x-ray and neutron scattering study of the single-layer manganese oxide $\text{La}_{1-x}\text{Sr}_{1+x}\text{MnO}_4$, a structural homologue of the well-studied high-temperature superconductor $\text{La}_{2-x}\text{Sr}_x\text{CuO}_4$, and the $n = 1$ end-member of the Ruddlesden-Popper series $\text{La}_{n(1-x)}\text{Sr}_{nx+1}\text{Mn}_n\text{O}_{3n+1}$. Our results for the doping dependence of the magnetic and structural properties give a refined understanding of the phase diagram of this material. We hope that these results will help guide the development of sophisticated theories for $\text{La}_{1-x}\text{Sr}_{1+x}\text{MnO}_4$. Since the complex CE phase observed near $x = 1/2$ is also relevant to the physics of the colossal magnetoresistance manganites ($n = 2$ and $n = \infty$), our detailed results for this part of the phase diagram of $\text{La}_{1-x}\text{Sr}_{1+x}\text{MnO}_4$ might furthermore contribute to a deeper understanding of the CMR phenomenon.

We would like to thank J.E Lorenzo, J.P Hill, and N. Nagaosa for helpful comments. SSRL is supported by the DOE Office of Basic Energy Sciences, Divisions of Chemical Sciences and Materials Sciences. The work at Stanford University was furthermore supported by the DOE under Contracts No. DE-FG03-99ER45773 and No. DE-AC03-76SF00515, and by NSF CAREER Award No. DMR9985067.

* Present Address: Department of Physics, University of Toronto, Toronto, Ontario M5S 1A7, Canada

† Present Address: NIST Center for Neutron Research, National Institute of Standards and Technology, Gaithers-

- burg, Maryland 20899
- [‡] Present Address: National Institute of Advanced Industrial Science and Technology, Tsukuba Central 2-2, Tsukuba, Ibaraki 305-8568, Japan
- [§] Present Address: Department of Biomedical Engineering, Emory University, Atlanta, GA 30322
- ¹ Y. Tokura and N. Nagaosa, *Science* **288**, 462 (2000).
 - ² E. Dagotto, T. Hotta, and A. Moreo, *Phys. Rep.* **344**, 1 (2001).
 - ³ M. B. Salamon and M. Jaime, *Rev. Mod. Phys.* **73**, 583 (2001).
 - ⁴ Y. Moritomo, Y. Tomioka, A. Asamitsu, Y. Tokura, and Y. Matsui, *Phys. Rev. B* **51**, 3297 (1995).
 - ⁵ W. Bao, C. H. Chen, S. A. Carter, and S.-W. Cheong, *Solid State Commun.* **98**, 55 (1996).
 - ⁶ Y. Moritomo, A. Asamitsu, H. Kuwahara, and Y. Tokura, *Nature* **380**, 141 (1996).
 - ⁷ B. J. Sternlieb, J. P. Hill, U. C. Wildgruber, G. M. Luke, B. Nachumi, Y. Moritomo, and Y. Tokura, *Phys. Rev. Lett.* **76**, 2169 (1996).
 - ⁸ Y. Murakami, H. Kawada, H. Kawata, M. Tanaka, T. Arima, Y. Moritomo, and Y. Tokura, *Phys. Rev. Lett.* **80**, 1932 (1998).
 - ⁹ J. M. Tranquada, B. J. Sternlieb, J. D. Axe, Y. Nakamura, and S. Uchida, *Nature* **375**, 561 (1995).
 - ¹⁰ C. H. Chen, S.-W. Cheong, and A. S. Cooper, *Phys. Rev. Lett.* **71**, 2461 (1993).
 - ¹¹ Y. Wakabayashi, Y. Murakami, Y. Moritomo, I. Koyama, H. Nakao, T. Kiyama, T. Kimura, Y. Tokura, and N. Wakabayashi, *J. Phys. Soc. Japan* **70**, 1194 (2001).
 - ¹² S. Larochele, A. Mehta, N. Kaneko, P. K. Mang, A. F. Panchula, L. Zhou, J. Arthur, and M. Greven, *Phys. Rev. Lett.* **87**, 095502 (2001).
 - ¹³ Y. Moritomo, A. Nakamura, S. Mori, N. Yamamoto, K. Ohoyama, and M. Ohashi, *Phys. Rev. B* **56**, 14879 (1997).
 - ¹⁴ C. Autret, R. Retoux, M. Hervieu, and B. Raveau, *Chem. Mater.* **13**, 4745 (2001).
 - ¹⁵ T. Kimura, K. Hatsuda, Y. Ueno, R. Kajimoto, H. Mochizuki, H. Yoshizawa, T. Nagai, Y. Matsui, A. Yamazaki, and Y. Tokura, *Phys. Rev. B* **65**, 020407 (2002).
 - ¹⁶ T. Nagai, T. Kimura, A. Yamazaki, T. Asaka, K. Kimoto, Y. Tokura, and Y. Matsui, *Phys. Rev. B* **65**, 060405 (2002).
 - ¹⁷ J.-C. Bouloux, J.-L. Soubeyroux, A. Daoudi, and G. Le Flem, *Mat. Res. Bull.* **16**, 855 (1981).
 - ¹⁸ J. B. Goodenough, *Phys. Rev.* **100**, 564 (1955).
 - ¹⁹ S. Ishihara and S. Maekawa, *Phys. Rev. Lett.* **80**, 3799 (1998).
 - ²⁰ M. Benfatto, Y. Joly, and C. R. Natoli, *Phys. Rev. Lett.* **83**, 636 (1999).
 - ²¹ I. S. Elfimov, V. I. Anisimov, and G. A. Sawatzky, *Phys. Rev. Lett.* **82**, 4264 (1999).
 - ²² P. Mahadevan, K. Terakura, and D. D. Sarma, *Phys. Rev. Lett.* **87**, 066404 (2001).
 - ²³ S. Ishihara and S. Maekawa, *Rep. Prog. Phys.* **65**, 561 (2002).
 - ²⁴ S. B. Wilkins, P. D. Spencer, P. D. Hatton, S. P. Collins, M. D. Roper, D. Prabhakaran, and A. T. Boothroyd, *Phys. Rev. Lett.* **91**, 167205 (2003).
 - ²⁵ S. S. Dhesi, A. Mirone, C. De Nadaï, P. Ohresser, P. Bencok, N. B. Brookes, P. Reutler, A. Revcolevschi, A. Tagliiferri, O. Toulemonde, et al., *Phys. Rev. Lett.* **92**, 056403 (2004).
 - ²⁶ K.J. Thomas, J.P. Hill, Y.-J. Kim, S. Greneier, P. Abbamonte, L. Venema, A. Rusydi, Y. Tomioka, Y. Tokura, D.F. McMorrow, and M. van Veenendaal, *condmat/0311553*.
 - ²⁷ D. J. Huang, W. B. Wu, G. Y. Guo, H. J. Lin, T. Y. Hou, C. F. Chang, C. T. Chen, A. Fujimori, T. Kimura, H. B. Huang, et al., *Phys. Rev. Lett.* **92**, 087202 (2004).
 - ²⁸ K. Yamamoto, T. Kimura, T. Ishikawa, T. Katsufuji, and Y. Tokura, *Phys. Rev. B* **61**, 14706 (2000).
 - ²⁹ P. Calvani, A. Paolone, P. Dore, S. Lupi, P. Maselli, P. G. Medaglia, and S.-W. Cheong, *Phys. Rev. B* **54**, R9592 (1996).
 - ³⁰ J. H. Jung, J. S. Ahn, J. Yu, T. W. Noh, J. Lee, Y. Moritomo, I. Solovyev, and K. Terakura, *Phys. Rev. B* **61**, 6902 (2000).
 - ³¹ T. Ishikawa, K. Ookura, and Y. Tokura, *Phys. Rev. B* **59**, 8367 (1999).
 - ³² M. Tokunaga, N. Miura, Y. Moritomo, and Y. Tokura, *Phys. Rev. B* **59**, 11151 (1999).
 - ³³ T. Ogasawara, T. Kimura, T. Ishikawa, M. Kuwata-Gonokami, and Y. Tokura, *Phys. Rev. B* **63**, 113105 (2001).
 - ³⁴ V. Kiryukhin, D. Casa, J. P. Hill, B. Keimer, A. Vigliante, Y. Tomioka, and Y. Tokura, *Nature* **386**, 813 (1997).
 - ³⁵ V. Kiryukhin, Y. J. Wang, F. C. Chou, M. A. Kastner, and R. J. Birgeneau, *Phys. Rev. B* **59**, 6581 (1999).
 - ³⁶ C. Baumann, G. Allodi, B. Büchner, R. De Renzi, P. Reutler, and A. Revcolevschi, *Physica B* **326**, 505 (2003).
 - ³⁷ J.-C. Bouloux, J.-L. Soubeyroux, G. Le Flem, and P. Haggenguller, *J. Solid State Chem.* **38**, 34 (1981).
 - ³⁸ S. Kawano, N. Achiwa, N. Kamegashira, and M. Aoki, *J. Phys. Colloq.* **49**, C8 829 (1988).
 - ³⁹ M. Bieringer and J. E. Greedan, *J. Mater. Chem.* **12**, 279 (2002).
 - ⁴⁰ J. Park, S. Lee, J.-G. Park, I. P. Swainson, Y. Moritomo, and H.-C. Ri, *Phys. Rev. B* **62**, 13848 (2000).
 - ⁴¹ C. S. Hong, E. O. Chi, W. S. Kim, N. H. Hur, K. W. Lee, and C. H. Lee, *Chem. Mater.* **13**, 945 (2001).
 - ⁴² P. Reutler, O. Friedt, B. Büchner, M. Braden, and A. Revcolevschi, *J. Cryst. Growth* **249**, 222 (2003).
 - ⁴³ R. J. Birgeneau, H. J. Guggenheim, and G. Shirane, *Phys. Rev. B* **1**, 2211 (1970).
 - ⁴⁴ M. F. Collins, *Magnetic Critical Scattering* (Oxford University Press, New York, 1989).
 - ⁴⁵ A. Zheludev, *ResLib 3.1* (Oak Ridge National Laboratory, 2001).
 - ⁴⁶ N. Furukawa and K. Hirota, *Physica B* **291**, 324 (2000).
 - ⁴⁷ K. Hirota, S. Ishihara, H. Fujioka, M. Kubota, H. Yoshizawa, Y. Moritomo, Y. Endoh, and S. Maekawa, *Phys. Rev. B* **65**, 064414 (2002).
 - ⁴⁸ R. R. P. Singh and M. P. Gelfand, *Phys. Rev. B* **52**, 15695 (1995).
 - ⁴⁹ Y. J. Kim, R. J. Birgeneau, F. C. Chou, M. Greven, M. A. Kastner, Y. S. Lee, B. O. Wells, A. Aharony, I. Y. Korenblit, A. B. Harris, et al., *Phys. Rev. B* **64**, 024435 (2001).
 - ⁵⁰ R. A. Cowley, G. Shirane, R. J. Birgeneau, and H. J. Guggenheim, *Phys. Rev. B* **15**, 4292 (1977).
 - ⁵¹ R. J. Birgeneau, J. Als-Nielsen, and G. Shirane, *Phys. Rev. B* **16**, 280 (1977).
 - ⁵² H. Ikeda and M. T. Hutchings, *J. Phys. C: Solid State Phys.* **11**, L529 (1978).
 - ⁵³ Y. S. Lee, M. Greven, B. O. Wells, R. J. Birgeneau, and G. Shirane, *Eur. Phys. J. B* **5**, 15 (1998).
 - ⁵⁴ H. G. Evertz, *Advances in Phys.* **52**, 1 (2003).

- ⁵⁵ B. Keimer, R. J. Birgeneau, A. Cassanho, C. Y. Chen, M. Greven, M. A. Kastner, A. Aharony, Y. Endoh, R. W. Erwin, and G. Shirane, *Phys. Rev. B* **46**, 14034 (1992).
- ⁵⁶ N. Elstner, A. Sokol, R. R. P. Singh, M. Greven, and R. J. Birgeneau, *Phys. Rev. Lett.* **75**, 938 (1995).
- ⁵⁷ C. J. Hamer, Z. Weihong, and J. Oitmaa, *Phys. Rev. B* **50**, 6877 (1994).
- ⁵⁸ I. Morgenstern and K. Binder, *Phys. Rev. B* **22**, 288 (1980).
- ⁵⁹ F. Matsubara and K. Katsumata, *Solid State Comm.* **49**, 1165 (1984).
- ⁶⁰ C. Dekker, A. F. M. Arts, and H. W. de WIJN, *Phys. Rev. B* **38**, 11512 (1988).
- ⁶¹ P. G. Radaelli, D. E. Cox, M. Marezio, and S.-W. Cheong, *Phys. Rev. B* **55**, 3015 (1997).
- ⁶² P. M. Woodward, D. E. Cox, T. Vogt, C. N. R. Rao, and A. K. Cheetham, *Chem. Mater.* **11**, 3528 (1999).
- ⁶³ D. N. Argyriou, H. N. Bordallo, B. J. Campbell, A. K. Cheetham, D. E. Cox, J. S. Gardner, K. Hanif, A. dos Santos, and G. F. Strouse, *Phys. Rev. B* **61**, 15 269 (2000).
- ⁶⁴ A. Daoud-Aladine, J. Rodriguez-Carvajal, L. Pinsard-Gaudart, M. T. Fernández-Díaz, and A. Revcolevschi, *Phys. Rev. Lett.* **89**, 097205 (2002).
- ⁶⁵ S. Grenier, J. P. Hill, D. Gibbs, K. J. Thomas, M. v. Zimmermann, C. S. Nelson, V. Kiryukhin, Y. Tokura, Y. Tomioka, D. Casa, et al., *Phys. Rev. B* **69**, 134419 (2004).
- ⁶⁶ S. Onada, Y. Motome, and N. Nagaosa, *cond-mat/0211520*.
- ⁶⁷ K. Miyano, T. Tanaka, Y. Tomioka, and Y. Tokura, *Phys. Rev. Lett.* **78**, 4257 (1997).
- ⁶⁸ C. H. Chen, S.-W. Cheong, and H. Y. Hwang, *J. Appl. Phys.* **81**, 4326 (1997).
- ⁶⁹ S. Mori, C. H. Chen, and S.-W. Cheong, *Nature (London)* **392**, 473 (1998).
- ⁷⁰ P. G. Radaelli, D. E. Cox, L. Capogna, S.-W. Cheong, and M. Marezio, *Phys. Rev. B* **59**, 14 440 (1999).
- ⁷¹ M. T. Fernández-Díaz, J. L. Martínez, J. M. Alonso, and E. Herrero, *Phys. Rev. B* **59**, 1277 (1999).
- ⁷² R. Wang, J. Gui, Y. Zhu, and A. R. Moodenbaugh, *Phys. Rev. B* **61**, 11 946 (2000).
- ⁷³ J. D. Axe, *Phys. Rev. B* **21**, 4181 (1980).
- ⁷⁴ T. Hotta, Y. Takada, H. Koizumi, and E. Dagotto, *Phys. Rev. Lett.* **84**, 2477 (2000).
- ⁷⁵ H. Yoshizawa, T. Kakeshita, R. Kajimoto, T. Tanabe, T. Katsufuji, and Y. Tokura, *Phys. Rev. B* **61**, R854 (2000).
- ⁷⁶ S. T. Bramwell and P. C. W. Holdsworth, *J. Phys.: Condens. Matter* **5**, L53 (1993).
- ⁷⁷ I. V. Solovyev, *Phys. Rev. Lett.* **91**, 177201 (2003).
- ⁷⁸ M. A. Krivoglaz, *X-ray and neutron diffraction in nonideal crystals* (Springer-Verlag, New York, 1996).
- ⁷⁹ L. Vasiliu-Doloc, S. Rosenkranz, R. Osborn, S. K. Sinha, J. W. Lynn, J. Mesot, O. H. Seeck, G. Preosti, A. J. Fedro, and J. F. Mitchell, *Phys. Rev. Lett.* **83**, 4393 (1999).
- ⁸⁰ S. Shimomura, N. Wakabayashi, H. Kuwahara, and Y. Tokura, *Phys. Rev. Lett.* **83**, 4389 (1999).
- ⁸¹ C. P. Adams, J. W. Lynn, Y. M. Mukovskii, A. A. Arsenov, and D. A. Shulyatev, *Phys. Rev. Lett.* **85**, 3954 (2000).
- ⁸² D. N. Argyriou, J. W. Lynn, R. Osborn, B. Campbell, J. F. Mitchell, U. Ruett, H. N. Bordallo, A. Wildes, and C. D. Ling, *Phys. Rev. Lett.* **89**, 036401 (2002).
- ⁸³ R. K. Li and C. Greaves, *J. Solid State Chem.* **153**, 34 (2000).
- ⁸⁴ S.-W. Cheong and H.Y. Hwang, *Colossal Magnetoresistance Oxides* (ed. Y. Tokura), Chapter 7. Gordon & Breach, 1999.
- ⁸⁵ J. van Elp, H. Sato, T. Kimura, T. Toda, Y. Okamura, Y. Tokura, and M. Taniguchi, *J. Phys. Soc. Japan* **69**, 2391 (2000).